Characterizing the Thermal Behavior of Pyrolytic Graphite Sheets (PGS) at Low Interface Pressures

by

Joushua G. Padilla

S.B. Mechanical Engineering, MIT, 2021

Submitted to the Department of Mechanical Engineering in Partial Fulfillment of the Requirements for the Degree of

MASTER OF SCIENCE

at the

MASSACHUSETTS INSTITUTE OF TECHNOLOGY

June 2023

© 2023 Joushua G. Padilla. All rights reserved.

The author hereby grants to MIT a nonexclusive, worldwide, irrevocable, royalty-free license to exercise any and all rights under copyright, including to reproduce, preserve, distribute and publicly display copies of the thesis, or release the thesis under an open-access license.

Authored by:	
	Department of Mechanical Engineering
	May 9, 2023
Certified by:	
<u> </u>	Julie Chalfant
	Research Scientist
	Thesis Supervisor
Certified by:	
	Chryssostomos Chryssostomidis
	Professor of Mechanical and Ocean Engineering
	Thesis Supervisor
Accepted by:	
	Nicolas Hadjiconstantinou
	Professor of Mechanical Engineering
	Graduate Officer

Characterizing the Thermal Behavior of Pyrolytic Graphite Sheets (PGS) at Low Interface Pressures

by

Joushua G. Padilla

Submitted to the Department of Mechanical Engineering in Partial Fulfillment of the Requirements for the Degree of Master of Science

ABSTRACT

As the United States Navy continues to pursue its goal of developing fully electric ships the cooling of the critical electronic components on board must be solved. One of these critical components is the integrated Power Electronics Building Block (iPEBB); a universal converter that is programmed for its specific application when installed. The iPEBB is a modular unit that can be easily swapped by a single person. This unique modularity has led the Navy to pursue the design of a dry interface liquid cooling system to cool the iPEBB. This means that no liquid can cross the boundary of the iPEBB and thus the cooling system must be separate.

In this thesis, an integral portion of the dry interface cooling solution, the thermal interface material (TIM) between the cold plate and iPEBB, was explored in a multitude of ways. First, commercially available TIMs were investigated for their thermal behavior at pressures less than 10 PSI as well as their structural qualities and usability metrics. Pyrolytic Graphite Sheets (PGS) were chosen to be investigated further. Second, a fourth order thermal conductivity model for PGS as a function of interface pressure was derived in the 0-10 PSI range. This model is important as it allows engineers to have conductivity inputs for the PGS in any thermal modeling done for future iterations of the iPEBB or in other systems where PGS is used as a TIM. Third, the design and testing of an experimental rig (PPR) for testing thermal interface materials under various average pressures and pressure profiles was presented. An empirical model was developed that demonstrates the effect that interface pressure profile has on component temperatures with PGS as the acting TIM between the cooling solution and the heated system. Finally, using the conductivity model, CFD simulations were run of PPR experiments. These simulation results were then compared to the results of the PPR experiments and it was discovered that using the conductivity model for PGS as an input in a CFD simulation is an effective way of modeling the contact resistance of PGS as a function of pressure. The effectiveness of the conductivity model – CFD simulation setup has a mean error of $1.4C \pm 1.3C$ between the simulation's outputted average resistor temperature and the actual average temperatures measured.

The experiments and simulations conducted in this thesis provide a blueprint for the necessary steps required to thermally model not only the iPEBB dry interface cooling system, but also other systems that might use PGS as a TIM, using CFD. The information in this thesis will also help researchers model the thermal behavior of the iPEBB cooling system once a clamping mechanism for the iPEBB structure is designed.

Thesis Supervisor: Julie Chalfant

Title: Research Scientist

Thesis Supervisor: Chryssostomos Chryssostomidis Title: Professor of Mechanical and Ocean Engineering

ACKNOWLEDGMENTS

I would like to express my deepest gratitude to Dr. Julie Chalfant and Professor Chryssostomos Chryssostomidis whose guidance, support, and expertise have been instrumental in the completion of this thesis. Their commitment to my academic growth and their consistent feedback have been invaluable in my growth these past two years. I would also like to thank Dr. Thomas Consi, who was my first UROP advisor on this project in 2019. Without his guidance, patience, and care, I would not be where I am in my academic and professional career.

To my mother and father, I am eternally grateful to the love and support you have shown me my entire life. You have pushed me to become the best version of myself while supporting me along the way. Your encouragement and love have been instrumental in my education especially these past two years.

To my brother I am thankful for the best role model and big brother anyone could ever ask for. Thank you for leading the way.

To my friends, Liam, Drew, and so many more, thank you for being there for me throughout not only these past two years, but the past six here at MIT. Your friendship has been a constant source of support and for that I cannot thank you enough.

I would also like to thank Rob Podoloff and the entire Tekscan team for their generosity and help during this entire process.

Finally, I would also like to thank the project's sponsors, MIT Sea Grant and the Office of Naval Research. This material is based upon research supported by the U.S. Office of Naval Research (ONR) under award number ONR N00014-21-1-2124 Electric Ship Research and Development Consortium; and by the National Oceanic and Atmospheric Administration (NOAA) under Grant Number NA22OAR4170126-MIT Sea Grant College Program. Without the financial support that was provided none of this would have been possible.

Table of Contents

Abstract	3
ACKNOWLEDGMENTS	5
Table of Contents	7
List of Figures	9
List of Tables	11
Chapter 1 Introduction	13
Chapter 2 Background	17
2.1 iPEBB	17
2.1.1 MOSFETS	18
2.2 Thermal Interface Materials	18
Chapter 3 Material Selection	21
3.1 Initial Thermal Interface Material Comparison	21
3.1.1 Design	21
Chapter 4 Thermal Interface Material Tester Rig	27
4.1 Design	28
4.2 Trials	30
4.3 Results	31
4.4 Discussion	32
Chapter 5 Pressure Proximity Rig	37
5.1 Design	37
5.1.1 Sensors	39
5.2 Trials	40
5.3 Average Pressure Results	41
5.4 Proximity Value Data	42
5.5 Cell to Cell Data Across Experiments	44
5.6 Corresponding Temperature Data	45
5.6.1 Results	48
5.7 Empirical Model Development	50
5.8 Accuracy of the Empirical Model	51
5.8.1 Discussion	
Chapter 6 CFD Simulation	
6.1 Design	

6.1.1 Results	55
6.1.2 Discussion	57
Chapter 7 Conclusions and Future Work	59
7.1 Conclusions	59
7.2 Future Work	59
References	61
Appendix	63
Appendix 1	
Appendix 2	65
Appendix 3	
Appendix 4	67

List of Figures

Fig. 1. The Navy iPEBB with dimensions annotated. Image courtesy of the Virginia Tech Center of Power and Energy Systems (CPES).
Fig. 2. The critical heat generation elements within the iPEBB are the MOSFET switches, depicted in the blue and red regions in the image. Image courtesy of the Virginia Tech Center of Power and Energy Systems (CPES).
Fig. 3. Graphic showing the experimental setup to conduct initial testing of TIMs
Fig. 4. Bottom up graphic showing thermocouple and heat source placement in initial TIM testing and selection process.
Fig. 5. Graphic showing the fluid system used to cool heated plate in TIM characterization experiments
Fig. 6. Bar charts showing average resistor temperature for each of the TIMs tested, at the three interface pressures.
Fig. 7. Image showing the breakdown of silicon based TIMs after being under compression and heat loads. This break down causes difficulty in clean up and is an undesirable performance trait for a TIM being used for the iPEBB
Fig. 8. Image showing PGS after multiple uses. Bends and deformation are present, however unlike the other TIMs tested, the PGS comes off in one piece and does not leave behind any mess
Fig. 9. Plot showing the thermal resistance vs. pressure curve from the PGS data sheet by Panasonic. The curve relevant to the experiments and testing performed in this thesis is the blue curve which characterizes the 0.2 mm thick PGS sheet. [10]
Fig. 10. Graphic showing side view of TIM Tester rig. This rig was used to complete thermal resistance vs pressure curve in the $0-10$ PSI range
Fig. 11. Plot showing completed thermal resistance vs pressure curve that integrates data taken from the Panasonic PGS data sheet (blue data) and the raw thermal resistance data collected with the TIM Tester rig (colored data)
Fig. 12. Thermal resistance vs pressure curve that includes the values from Table 4 in the $0-10$ PSI range with the values extracted from the Panasonic PGS datasheet. [10]
Fig. 13. Plot showing compressibility curve of PGS as a function of pressure. [10]
Fig. 14. Plot showing derived compression factor vs pressure curve that would be used to derive thermal conductivity of PGS as a function of pressure
Fig. 15. Thermal conductivity vs pressure curve (red) derived from the data points seen in magenta and blue.

Fig. 16. CAD model of Pressure Proximity Rig	38
Fig. 17. Pressure Proximity Rig Exploded View	38
Fig. 18. Pressure Proximity Rig with cross bars and supports	39
Fig. 19. Pressure profiles from two of the repeatability experiments with identical thermal and compressive loads.	
Fig. 20. Average pressure and standard deviations for five experiments to determine rig repeatability	42
Fig. 21. Proximity values from four resistors in each of five experiments	43
Fig. 22. Average proximity values for each of the four resistors across all five experiments	43
Fig. 23. Average profile residuals for each experiment.	45
Fig. 24. Average steady state resistor temperatures across the five repeatability experiments 4	46
Fig. 25. The average residuals of resistor temperature for each experiment.	47
Fig. 26. Pressure profiles created using the pressure proximity rig showing even pressure across the full surface (top image), pressure concentrated along the left side of the rig (middle image), and pressure concentrated across the top of the rig (bottom image)	
Fig. 27. Pressure profile and individual resistor temperatures for a single experiment,	49
Fig. 28. Individual resistor temperatures plotted versus average pressure across the full plane for 21 individual experiments	
Fig. 29. Predicted and actual resistor temperatures plotted versus P_{avg} (left) and τ (right)	52
Fig. 30. Mesh quality and statistics (left) along with image of mesh applied to CAD of PPR 5	55
Fig. 31. Domain convergence plots for each of the four simulations run	56
Fig. 32. Image of temperature solution field for 4.3 PSI simulation case	56

List of Tables

Table 1. List of TIM's tested with their associated thicknesses and thermal conductivities	21
Table 2. List of parameters held constant in TIM characterization experiments	23
Table 3. Pugh Chart comparing all TIMs explored in selection process	26
Table 4. List of masses used in TIM Tester rig to apply interface pressure to PGS	29
Table 5. Corresponding pressures and average thermal resistances at said pressures from TIM Tester experiments	
Table 6. List of polynomial constants for fourth order conductivity model of PGS	35
Table 7. Sensors used in PPR with associated uncertainties and ranges	40
Table 8. Fluid and PGS properties in four reference experiments and simulations	54
Table 9. Solid body material properties used in simulations	54
Table 10. Average resistor temperature results from each simulation	57
Table 11. Comparison of simulation results and reference experimental results	57

Chapter 1 Introduction

The Navy-funded Electric Ship Research and Development Consortium (ESRDC) works to advance technologies and concepts for electric ships. By electrifying ships, the Navy has the flexibility to control and direct energy where it is needed within a vessel [1]. One part of this effort is the development of the Navy integrated Power and Energy Corridor (NiPEC), which is a modular entity that encapsulates all the power handling requirements of a shipboard power and energy distribution system including transmission, conversion, protection, isolation, control and storage [2]. The basic component or least replaceable unit of the NiPEC is the integrated Power Electronics Building Block (iPEBB), which is envisioned to be a universal converter that is programmed for the specific application when installed [3]. iPEBBs may be combined in series or parallel to increase the voltage or current as required. The NiPEC will contain many, possibly hundreds of, iPEBBs. The iPEBB design is portable and replaceable, so the crew can easily swap out damaged or malfunctioning iPEBBs but leave the surrounding system in place if the equipment is still viable [2].

A sample iPEBB is shown in Fig. 1. The iPEBB is designed to be a rectangular shape and is depicted with outer substrate walls constraining the inner electrical components. This modular design allows the iPEBB to be easily ordered in expandable, compact grids within the power corridor of the ship [4].

One of the significant challenges involved in implementing an iPEBB-based power corridor is managing the thermal loads. A single iPEBB generates between 6000 and 11000 W of waste heat and that heat must be removed in order to maintain the temperature of the internal components of the iPEBB below 150 C. Many solutions have been explored and considered. Air cooling solutions are limited in performance due to the low density, thermal conductivity, and specific heat of air. As heat loads increase, the amount of air or liquid required for cooling increases; in this example with 6kW of waste heat, the required pumping power for forced convection cooling, allowing a tendegree Celsius temperature rise in the air, is 214W, whereas the pumping power for water as a heat transfer fluid with the same allowed temperature rise is only 0.35W. This calculation can be found in Appendix 1. Another factor that causes the air-cooling solution to be undesirable is the weight associated with adding a large aluminum heat sink to the top and bottom surfaces of the iPEBB. The iPEBB must remain under 16 kgs; therefore, installing heat sinks to the exterior of the iPEBB causes the weight of the iPEBB to exceed this limit. These reasons led to the further exploration of indirect liquid cooling.

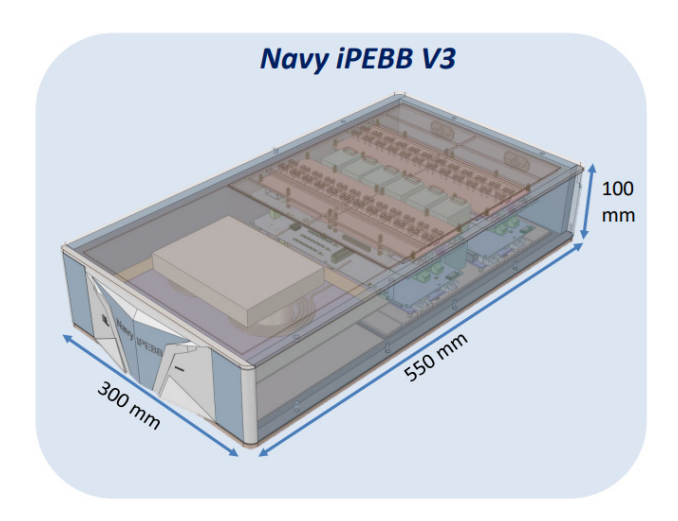


Fig. 1. The Navy iPEBB with dimensions annotated. Image courtesy of the Virginia Tech Center of Power and Energy Systems (CPES).

In the past couple of years, the ESRDC has pursued a cabinet cooling design concept that implements dry interface liquid cooling as the vehicle for thermal management of the iPEBB. The cabinet cooling concept was born out of the key design requirement that no liquid connections can be attached to the iPEBB itself because of its need to be modular and easily replaceable. This constraint causes the thermal management of the iPEBB to become more complex and challenging as direct component cooling is not possible.

Dry interface liquid cooling is accomplished via the use of a cold plate that is in series thermally with the iPEBB and that uses liquid convection to remove heat from the iPEBB. This concept evolved from the constraint that no liquid can enter the iPEBB structure itself. Thus, heat must be removed from the available outer surfaces of the iPEBB. The cold plate is incorporated into the cabinet system of the iPEBB stack. This presents the issue of contact resistance between the cold plate and the iPEBB, as the two cannot be permanently secured to one another.

A common way to lower contact resistance between two interfaces is through the use of a thermal interface material. Thermal interface materials (TIMs) are inserted between an electronic component that needs to be cooled and the cooling solution such as a heat sink in order to lower the contact resistance by filling in the small gaps between the surfaces when they are placed under a compressive load. This compressive load forces the thermal pad to fill the interstitial gaps between the components, supplying a conductive pathway where an air gap would have been. These interface materials vary in conductivity, Young's modulus, Poisson's ratio, as well as in the selected thickness.

The iPEBB application is somewhat different from the typical thermal interface application. Usually, thermal interface materials are used for a fairly small surface area, are applied in a clean environment in a factory, and are left in place for the lifetime of the equipment. The large interface area of the iPEBB application means that any significant required pressure for TIM performance will correspond to a very large required force on the installed iPEBB. There is also a challenge in providing even pressure across this full surface area. The plug-and-play nature of the iPEBB means that the TIM must be structurally robust so that it neither deteriorates with repeated installation nor leaves a fouled surface area in the cabinet where the replacement iPEBB will be installed. Since the TIM will be exposed to and installed in the shipboard environment, there is the possibility of

the intrusion of grit in the interface surface. The TIM is intended to be pre-installed on the surface of the iPEBB, therefore must be lightweight to meet the weight constraints on the component.

One TIM material is the Pyrolytic Graphite Sheet (PGS). PGS was selected for further investigation due to its high in-plane conductivity, its light weight and structural integrity, and its usability compared to other Thermal Interface Materials. These qualities make it a high-ranking candidate for the modular iPEBB system.

To determine the effectiveness and applicability of PGS as a thermal interface material between the iPEBB and the cold plate proposed in the dry interface liquid cooling design, several sets of experiments were conducted.

The first set of experiments, discussed in Chapter 4, were conducted using the TIM Tester rig. This rig was designed to determine the thermal resistance and conductivity of PGS as a function of the interface pressure within the 0-10 PSI range, a range that had not yet been quantified. This curve provides conductivity values for PGS as a function of pressure, a new input that would be very helpful in assigning material properties in Computational Fluid Dynamics (CFD) simulations.

The second set of experiments, discussed in Chapter 5, were conducted to determine how various pressure profiles affect the thermal behavior of the PGS and the impact on the heating elements of the iPEBB. To accomplish this exploration, a second rig was designed called the Pressure Proximity rig. The data collected from these experiments can be used to better understand the multidimensional heat transfer that occurs under different pressure loading profiles and how PGS performs under these different load cases. The output of these experiments was used to create an empirical model with two independent variables: average interface pressure and pressure proximity value, along with a single dependent variable: component temperature. This empirical model was compared to another set of randomized pressure profile experiments on the pressure proximity rig to determine its predictive capacity.

Finally, in Chapter 6, implementing the data from both experimental rigs, CFD simulations were run on a CAD model of the Pressure Proximity rig, with the same loading and parameters as seen in the experiments conducted. The PGS' thermal conductivity input was determined by the thermal conductivity vs. interface pressure curve produced using the TIM Tester rig. These simulations were run for four different cases, all with different average interface pressures. The results were then compared to the actual data from these runs as well as to the empirical model discussed earlier.

These experiments and simulations all allow the ESRDC to make recommendations on whether PGS should be used as a thermal interface material and, if so, under what conditions for the best possible thermal performance, ensuring the chosen thermal management system can meet all of the thermal loads necessary.

Chapter 2 Background

2.1 iPEBB

The iPEBB is designed to be easily transportable through narrow passageways and ladders within the ship, which leads to a necessary weight requirement of less than 16 kg. This is a significant restriction because the current weight of the iPEBB V3 is 14.1 kg, thus severely limiting the scope of viable cooling options. To meet the weight requirement, the cooling system must be small and compact (under 1.9 kg); if this is not possible, the iPEBB would likely have to shed weight to meet its target value. A possible solution to the weight constraint is to focus the cooling mechanisms to critical areas that generate heat.

The current Navy iPEBB is designed to be 300mm x 550mm x 100mm, as shown in Fig. 1. It is important to note that the dimensional requirements are not finalized, and the shape of the iPEBB could change in future iterations. Additionally, the iPEBB dimensions do not include any supplemental external parts needed by the cooling system. While the size of the cooling system is not mandated, the volume of the cooling mechanism contributes to the power density of the NiPEC and should therefore be minimized while remaining cost- and complexity-conscious.

The iPEBB is an enclosed box with electrical components that generate heat as they perform various processes to supply power to different operations within the ship. This is problematic because the heat generated within the box can only be transferred out into the environment through conduction, and a cooling mechanism is essential to increase the rate of heat transfer out of the system. If heat cannot be transferred out of the iPEBB efficiently, the operational power of the iPEBB must be decreased or components within the shell are at risk of damage. The cooling system must control the temperature of the most critical heat producing elements of the iPEBB: the MOSFET switches and the transformer, shown in Fig. 2. These elements produce essentially all the waste heat in the iPEBB and will subsequently have the highest temperatures within the iPEBB.

By imposing a rack-level cooling design on the top and bottom of the iPEBB, we can focus on cooling the critical concentrated heat loads generated by the rows of switches and the transformer. The MOSFET switches are depicted in the blue and red regions in Fig 2. It is important to note that the image in Fig 2 only displays the cross-sectional view of the top shell of the iPEBB, but there is a mirrored image on the bottom shell. This means that there is a total of four rows of switches within the iPEBB. Moreover, there is only one transformer located in the iPEBB. The top and bottom shell surfaces are denoted as the location for Rack Level Cooling; the cooling method will access these surfaces to remove heat produced by the MOSFET switches and the transformer [4].

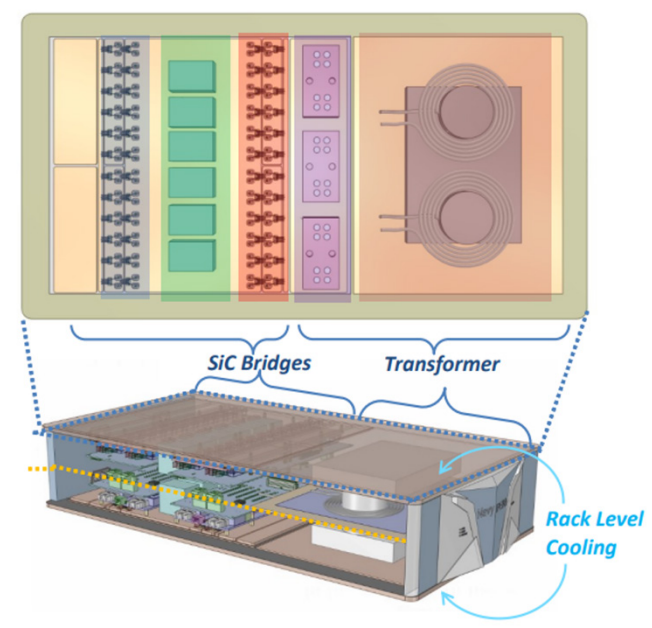


Fig. 2. The critical heat generation elements within the iPEBB are the MOSFET switches, depicted in the blue and red regions in the image. Image courtesy of the Virginia Tech Center of Power and Energy Systems (CPES).

2.1.1 MOSFETS

The critical heat-producing elements of the iPEBB are the SiC MOSFET bridges that are located inside the top and bottom shells. Both top and bottom substrates have two rows of switches consisting of 24 MOSFETs in each row, for a total of 48 switches per substrate and 96 switches in the entire iPEBB. The switches are in close proximity to one another which can lead to a significant heat concentration that will potentially deteriorate the electrical capability of the switches. As shown in the figure, the switches are spaced 2cm apart on center, which will lead to heat spreading effects between the switches [4].

The MOSFETs used in this application are approximated by a square prism shape with a thickness of 1mm and a side length of 0.8cm. Each MOSFET produces 100 W of waste heat, for a heat flux of 153 W/cm².

SiC MOSFETs generally have peak operational temperatures ranging between 150 to 200 C; thus, the current study will proceed with the goal of keeping each switch below 150 C. This is essential not only in the design for the extreme scenarios, but also because MOSFETs with lower operating temperatures are less expensive.

2.2 Thermal Interface Materials

Thermal Interface Materials (TIMs) are inserted between an electronic component that needs to be cooled and the cooling solution such as a heat sink in order to lower the contact resistance.

There are many different types of TIMs, ranging from the more standard and available siliconbased pads, to two-phase materials, to the material explored in this thesis: graphite-based sheets. Each material has distinct advantages and disadvantages; thus, depending on the context of the system being examined and its design requirements, different TIMs will be better than others for a given application. In this thesis, the TIM that was explored in depth is the Pyrolytic Graphite Sheet (PGS). PGS is a synthetically produced material with a thin graphite film structure and high thermal conductivity. PGS is manufactured by heating a polymer film to its decomposition temperature in a vacuum. The film carbonizes then graphitizes, leaving a highly oriented graphite material. The graphene sheets are stacked on top of one another, promoting high in-plane thermal conductivity and thus heat spreading in the plane [5].

PGS is durable and can be reused many times without falling apart unlike many silicon-based or acrylic-based thermal interface materials. This quality makes it ideal for the modularity associated with the iPEBB stacks, so long as the PGS can meet the thermal constraints of the iPEBB and cooling system.

Chapter 3 Material Selection

3.1 Initial Thermal Interface Material Comparison

3.1.1 Design

The motivation for this thesis was developed when examining the thermal performance of various thermal interface materials at low compressive loads. First, the multidimensional thermal behavior of various commercially available Thermal Interface Materials (TIMs) was examined at low interface pressures. Most TIMs are used on fairly small areas with high compressive loads of around 10-30 PSI. Because of the small area, high forces are not required to achieve high pressures. This means that a compression method more complex than simple bolts is not necessary. The initial series of experiments examined the thermal behavior of five TIMs at 0.42 PSI, 1.25 PSI, and 2.50 PSI across a contact area of 36 sq in, with a 5.6 lpm flowrate of 26 C water through the cold plate. Properties of the TIMs used can be seen in Table 1.

Table 1. List of TIM's tested with their associated thicknesses and thermal conductivities

TIM	Advertised Thermal Conductivity [W/m-K]	Thickness [mm]
PGS	28 [10]	0.2
Graphite Resin	13 [11]	1.5
Silicon Elastomer	12.6 [12]	1.5
Non-silicon	2.1 [13]	1.5
No TIM	-	-

The rig used in these experiments was simple and relied on a known mass and known cross sectional area to calculate an average pressure. The design of the rig can be seen in Fig. 3 and Fig. 4

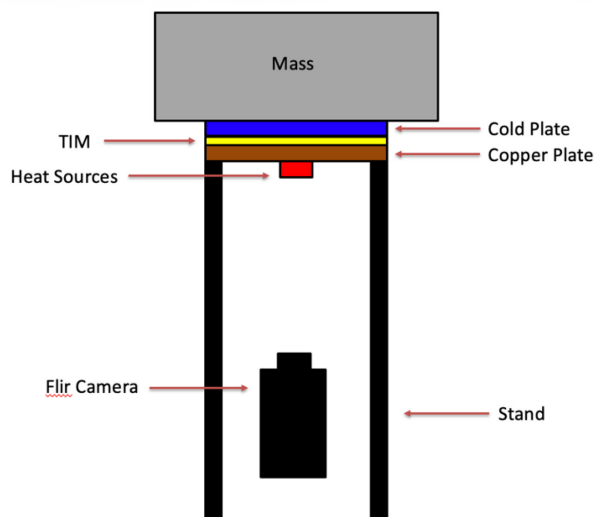


Fig. 3. Graphic showing the experimental setup to conduct initial testing of TIMs

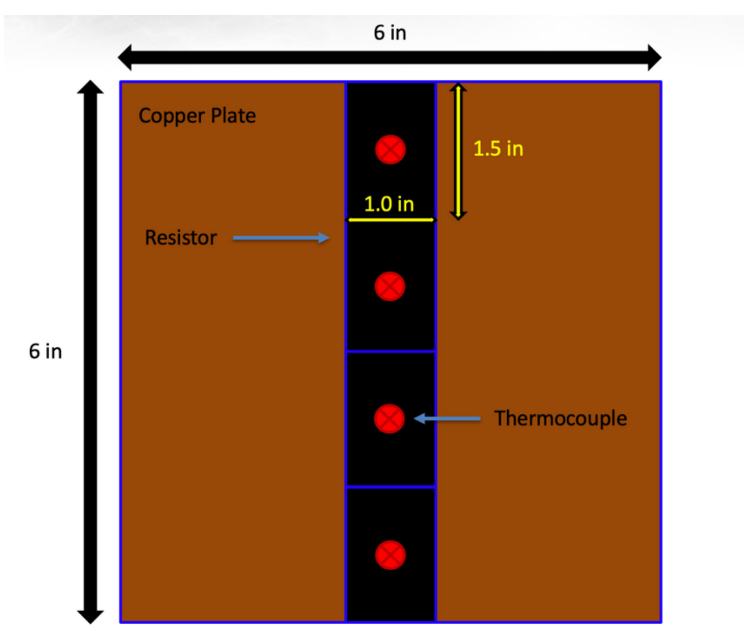


Fig. 4. Bottom up graphic showing thermocouple and heat source placement in initial TIM testing and selection process.

The rig consisted of very few parts and relied on mass for the compressive load at the thermal interface between the heated copper plate, where the resistors were mounted, and the water-cooled cold plate. The cold plate was supplied chilled water at 26 C from a water tank, whose water was chilled by a Thermo-fisher circulating bath water chiller. A diagram of the fluids system can be seen in Fig. 5.

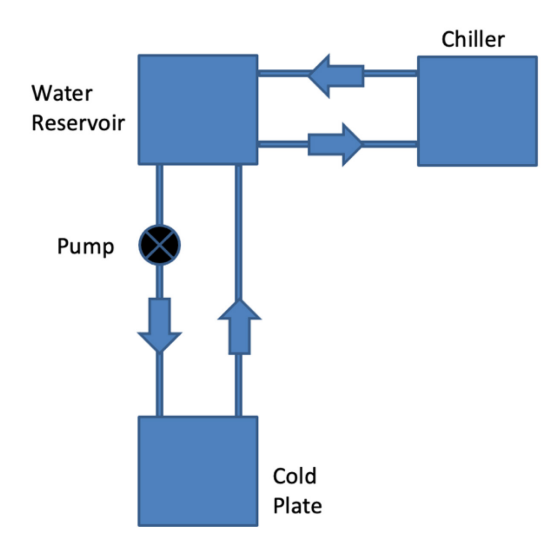


Fig. 5. Graphic showing the fluid system used to cool heated plate in TIM characterization experiments

The mass was varied three times while the remaining parameters of the system remained constant. Those parameters are listed in Table 2.

Table 2. List of parameters held constant in TIM characterization experiments

Parameter	Value
Heat Load (W)	255
Water Flowrate (LPM)	5.6
Flow Inlet Temperature (C)	26
Ambient Temperature (C)	27

In each experiment, the temperature of each resistor was measured via thermocouples. Thermocouples were also used to measure the ambient temperature, inlet temperature of the cold plate, and outlet temperature of the cold plate. A flowmeter was used to measure the flow rate of the water in the system. The critical measurement used to judge the performance of the TIMs at each interface pressure was the temperature recorded by the thermocouples directly attached to the resistors. For each TIM, the average steady state temperatures of the resistors are shown in Fig. 6.

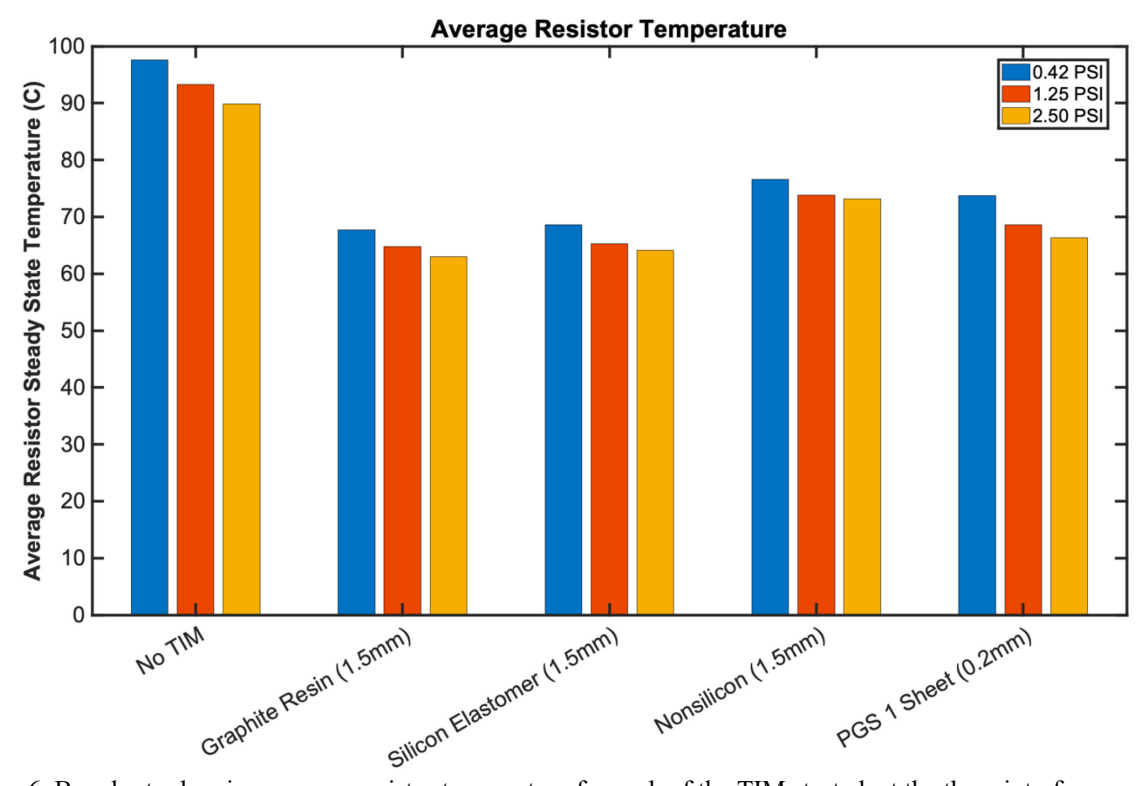


Fig. 6. Bar charts showing average resistor temperature for each of the TIMs tested, at the three interface pressures.

The bar chart in Fig. 6 above, shows that the Pyrolytic Graphite Sheet (PGS) sheet performs comparably to the other TIMs. Compared to the case with no TIM, the PGS, averaged over the three different pressures, resulted in a resistor temperature that was $24.1C \pm 0.6C$ cooler. When compared to the best performing TIM of the bunch, the Graphite Resin, the PGS was outperformed by an average of $4.4C \pm 1.4C$. Despite this, The PGS sheet was still able to outperform the non-silicon TIM by an average of $5.0C \pm 2.0C$.

As the thermal performance of the PGS is similar to that of standard TIMs, qualitative comparisons of the materials were also made, specifically about their structural integrity before and after the compressive loads were applied, as well as their usability, which can be described as how difficult they are to apply and remove from the interface. These properties are crucial for the TIM that will be used in the cooling system of the PEBB because of its modular nature. The standard TIMs are both very difficult to apply and remove. Much like a phone screen protector unless applied very carefully, by brushing the surface and ensuring perfect alignment, air bubbles, grit, and misalignment can occur very easily. These issues all can adversely affect the thermal performance of the entire cooling system. Likewise, many issues are present during the removal of the three other TIMs. Their soft, gummy nature makes removal time-consuming and messy. After compressed and heated, the standard interface materials lose their structural integrity; thus, when they are removed, they come off in pieces and leave behind a gummy adhesive-like film. The consequences can be seen in Fig. 7.



Fig. 7. Image showing the breakdown of silicon based TIMs after being under compression and heat loads. This break down causes difficulty in clean up and is an undesirable performance trait for a TIM being used for the iPEBB.

Unlike the other TIMs, the PGS did not have any of these issues. Application of the PGS is similar to placing a sheet of paper or very thin cardboard on a flat surface. Removal is also very easy. Because the PGS is a more rigid sheet, the compressive forces and heating do not cause it to break down structurally. Instead, the sheets remain intact, so removal of the PGS is just as easy as application. The structural integrity of the PGS can best be seen in the two images shown in Fig. 8. The photo on the left shows the sheet out of the box, and the photo on the right shows the sheet after use.

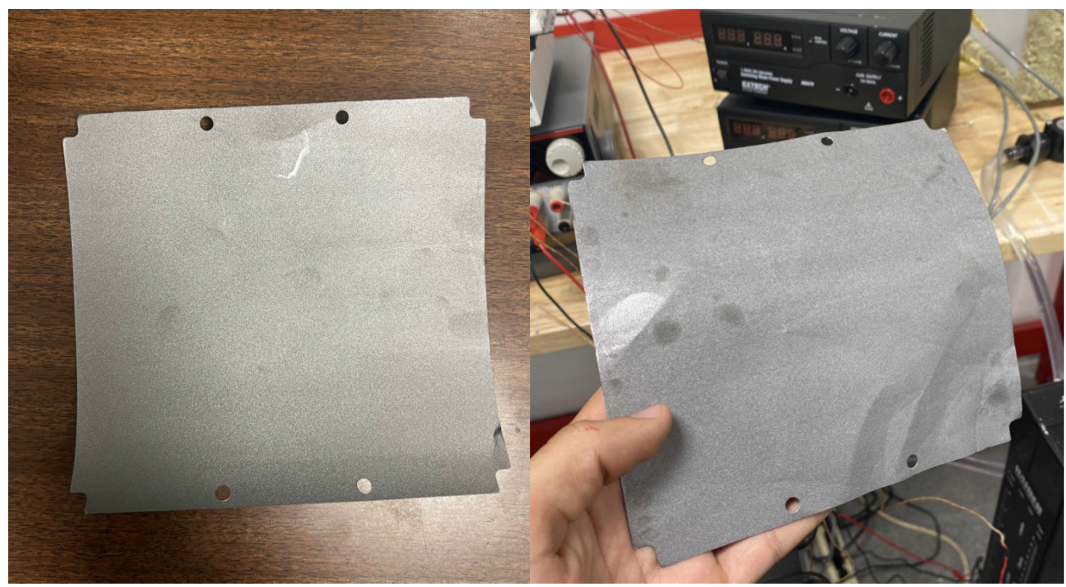


Fig. 8. Image showing PGS after multiple uses. Bends and deformation are present, however unlike the other TIMs tested, the PGS comes off in one piece and does not leave behind any mess.

This initial set of experiments were conducted to explore a wide array of thermal interface materials. These materials were examined for both their ability to transfer heat at the cold-plate-to-heated-plate interface as well as their structural capabilities and usability when both placing the TIMs as well as removing them after use.

Table 3. Pugh Chart comparing all TIMs explored in selection process

TIM	Instillation	Removal	Durability	Thermal	Total
				Performance	
Silicon	0	0	0	0	0
Elastomer					
<u>PGS</u>	<u>1</u>	<u>1</u>	<u>1</u>	<u>0</u>	<u>3</u>
Graphite Resin	0	0	0	1	1
Non-silicon	0	0	0	0	0
No TIM	1	1	1	-1	2

These initial experiments showed that the PGS could perform thermally, just as well as the more standard thermal interface materials however its usability was far above the other TIMs tested. These results can be seen above in the Pugh Chart that compares the TIMs on four different qualities. Pugh Charts are commonly used method to analyze ideas and to determine the optimal choice by comparing the ideas of interest in a quantitative way. The PGS ended up scoring the highest of all the commercially available options for the iPEBB use case. The combination of qualities in the chart points to PGS as the best candidate TIM for further exploration for the iPEBB dry interface cooling system.

Chapter 4 Thermal Interface Material Tester Rig

A critical step to making predictions for the thermal behavior of the iPEBB with the proposed dry interface cooling method is defining the thermal behavior, namely the thermal resistance, of PGS at pressures lower than 10 PSI. This pressure upper bound is critical due to the structural design constraints of the iPEBB's cabinet stack system. To limit the complexity of the clamping mechanism, it is ideal for the dry interface cooling system to operate successfully at low pressures, limiting the need for high-strength actuators to apply large interface pressures between the iPEBB and the cold plate. Manufacturer's data sheets for the PGS material being explored only provide data at pressures higher than 50 kPa (7.25 psi). [10] Due to this lower bound on available data, a rig (the TIM Test Rig) was designed to experimentally determine the thermal resistance of PGS in the 0 – 10 PSI range.

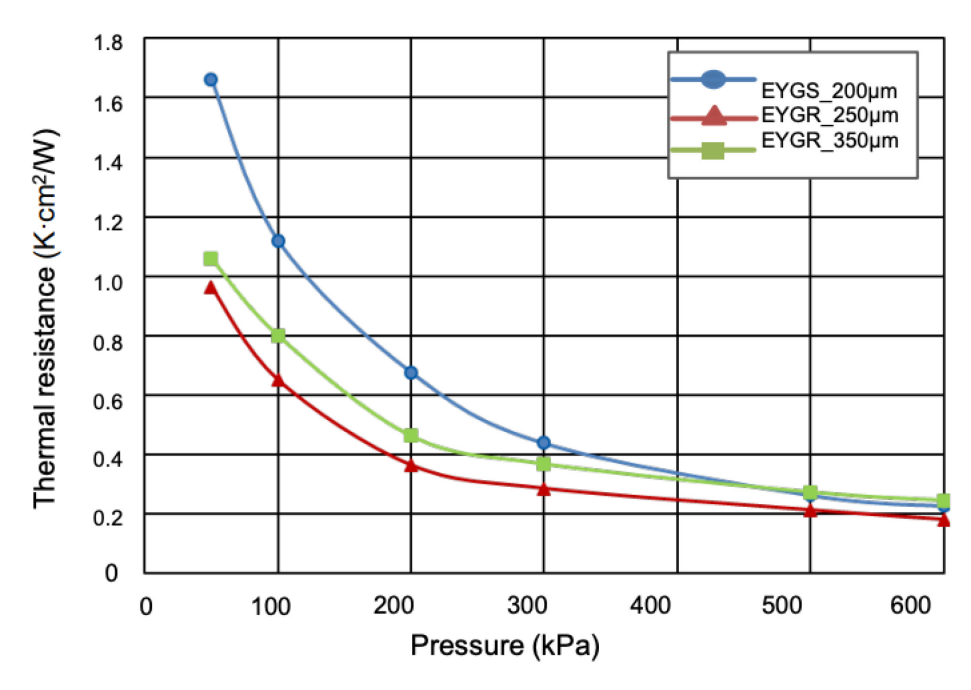


Fig. 9. Plot showing the thermal resistance vs. pressure curve from the PGS data sheet by Panasonic. The curve relevant to the experiments and testing performed in this thesis is the blue curve which characterizes the 0.2 mm thick PGS sheet. [10]

4.1 Design

The TIM Tester rig was designed to experimentally derive the thermal resistance of PGS in the 0-10 PSI range. Its design was based off of a rig built by Hayden Carlton to determine thermal properties of thermal interface paste [9]. His rig was designed specifically to meet the ASTM 5470-06 standard. The rig used in this thesis, while based on Carlton's rig, was not identical and did not have the necessary instrumentation to meet the ASTM 5470-06 standard [18]. The TIM Tester rig derived thermal resistance values of PGS very simply by supplying a heating element, known mass, two identical cylinders of aluminum, a tab of 0.2 mm thick PGS, a liquid-cooled cold plate, insulation, and k-type thermocouples.

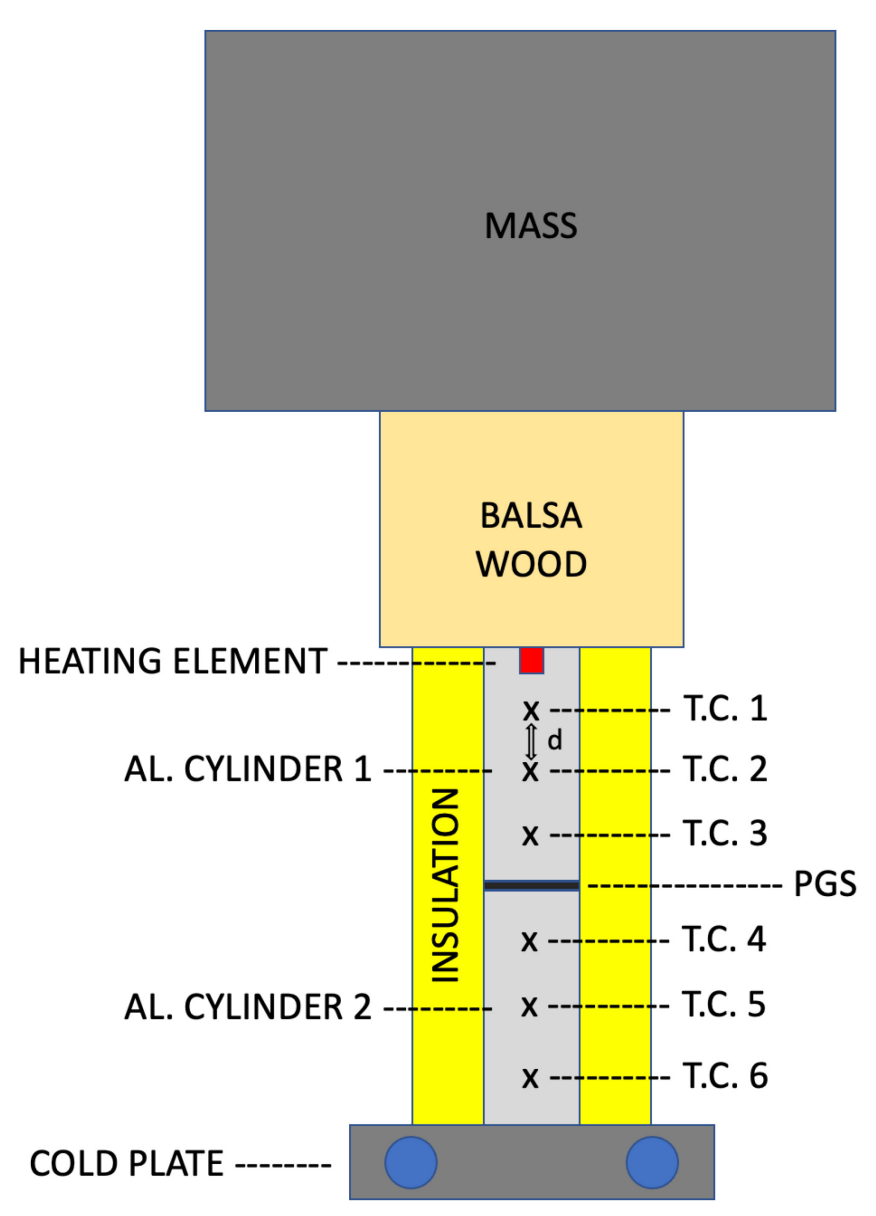


Fig. 10. Graphic showing side view of TIM Tester rig. This rig was used to complete a thermal resistance vs. pressure curve in the 0-10 PSI range.

A heating element was inserted into the top face of the upper aluminum cylinder. This supplies the heat load that is used to introduce a temperature gradient in the aluminum – PGS stack, allowing a PGS thermal resistance to be calculated. On the very bottom of the stack, at the bottom face of the second aluminum cylinder, a cold plate is placed. This cold plate prevents the system from overheating while also ensuring a temperature gradient in the stack that is large enough such that it is measurable. On the top face a large block of balsa wood was bolted to the first aluminum cylinder. This block of wood acted as insulation between the aluminum and steel masses as well as a flat, stable platform for the masses to be seated on when pressure was applied. The insulation on the sides was made up of two materials; balsa wood and foam. The balsa wood was shaped to act as a collar to ensure the centers of the cylinders were aligned exactly the same every time pressure was applied, while the foam acted as another layer to fill in gaps ensuring minimal losses to the ambient air. The PGS tab was cut to the cross-sectional dimensions of the cylinder ensuring good contact between the two inner faces of the aluminum cylinders. Mass was added to the system by stacking steel plates at the top. The individual plates were cut from large pieces of steel. The masses used in these experiments are listed in Table 4.

Table 4. List of masses used in TIM Tester rig to apply interface pressure to PGS

Trial Number	Mass Used (g)	Mass Used (lbs)	Resulting Pressure (PSI)
1	678	1.4947	0.8493
2	1649	3.6354	2.0656
3	2928	6.4551	3.6677
4	4194	9.2462	5.2535
5	6725	14.8261	8.4239

The masses were placed such that their cumulative center of mass was directly over the centerline of the first aluminum cylinder. This ensured no tipping of the stack or any non-symmetric pressure behavior at the PGS interface.

The thermocouples in the stack were placed at seven locations; six were in the aluminum cylinders, and the seventh measured the ambient air temperature of the system. Within the top cylinder, the first and second thermocouples were placed 1 inch apart and the second and third thermocouples were also placed 1 inch apart. Finally, in the first cylinder, the distance between the third thermocouple and bottom face was also 1 inch.

Now for the second cylinder, the fourth thermocouple was placed 1 inch from the top side. The fifth and sixth thermocouples were placed one inch apart from each other. By maintaining the distances between the thermocouples at these one-inch increments, the thermal resistances between the thermocouples could be compared very easily.

Thermal resistance can be calculated in two ways. The first, which was used in these experiments, is based on knowing the heat transfer through the system, and the temperatures between two points in that system. The second uses dimensions of the system and the associated thermal conductivity in that system.

In these experiments, the equation used to calculate the thermal resistance between any two thermocouples was

$$R_{th} = \frac{T_{n+1} - T_n}{O} \tag{1}$$

The region of interest in this case was the region between thermocouples three and four. This is where the PGS was placed between the two cylinders. From this region, the goal is to find the thermal resistance of the PGS under different pressure loads. To calculate this, there would be a two-step process. First the thermal resistance between thermocouples 3 and 4 was calculated via

$$R_{GAP} = \frac{T_4 - T_3}{O} \tag{2}$$

where Q is the heat load from the heating element, which in every experiment using the TIM Tester was 42 W. It is crucial to note, R_{GAP} is a thermal resistance associated with a distance between thermocouples of 2 inches. To find R_{PGS} a new R_{BAR} , would be introduced. R_{BAR} is the thermal resistance of a 2-inch section of aluminum bar without the PGS interface. In the case of these experiments, R_{BAR} would be the region between thermocouples 1 and 3. Thus, R_{BAR} would be calculated via,

$$R_{BAR} = \frac{T_3 - T_1}{O} \tag{3}$$

Now with R_{GAP} , and R_{BAR} calculated from the steady state thermocouple measurements, R_{PGS} as a function of the interface pressure could be calculated. This calculation would be done by Subtracting R_{BAR} from R_{GAP} . This can be seen in,

$$R_{PGS} = R_{GAP} - R_{BAR} \tag{4}$$

This calculation yields the thermal resistance of PGS as a function of its interface pressure.

4.2 Trials

To experimentally derive the thermal resistance vs. interface pressure curve for PGS, specifically at low pressures, four sets of experiments were conducted. Each set consisted of five different thermal resistance measurements at five different interface pressures. This yielded 20 different thermal resistance values spread across the five pressures, spanning 0-10 PSI. The four resistance measurements at a given pressure were then averaged to yield the final data point used to create a thermal resistance versus pressure curve.

Once the thermal resistance data of the PGS was gathered at the five pressures in the 0-10 PSI range, this low-pressure data was combined with the values supplied by the 0.2 mm PGS data sheet seen in the Panasonic data sheet plot above to create a full thermal resistance vs interface pressure curve that included these low-pressure values.

4.3 Results

As mentioned earlier, 20 distinct thermal resistance measurements were recorded at five different pressures in the 0-10 PSI range. These five pressures were: 0.8493 PSI, 2.0656 PSI, 3.6677 PSI, 5.2535 PSI, and 8.4239 PSI. The raw data from these runs can be seen below and is listed in Appendix 2, where the thermal resistances that were measured from the experiments conducted in this thesis are colored green, red, cyan, and magenta while those taken from the data sheet of the PGS used are in blue.

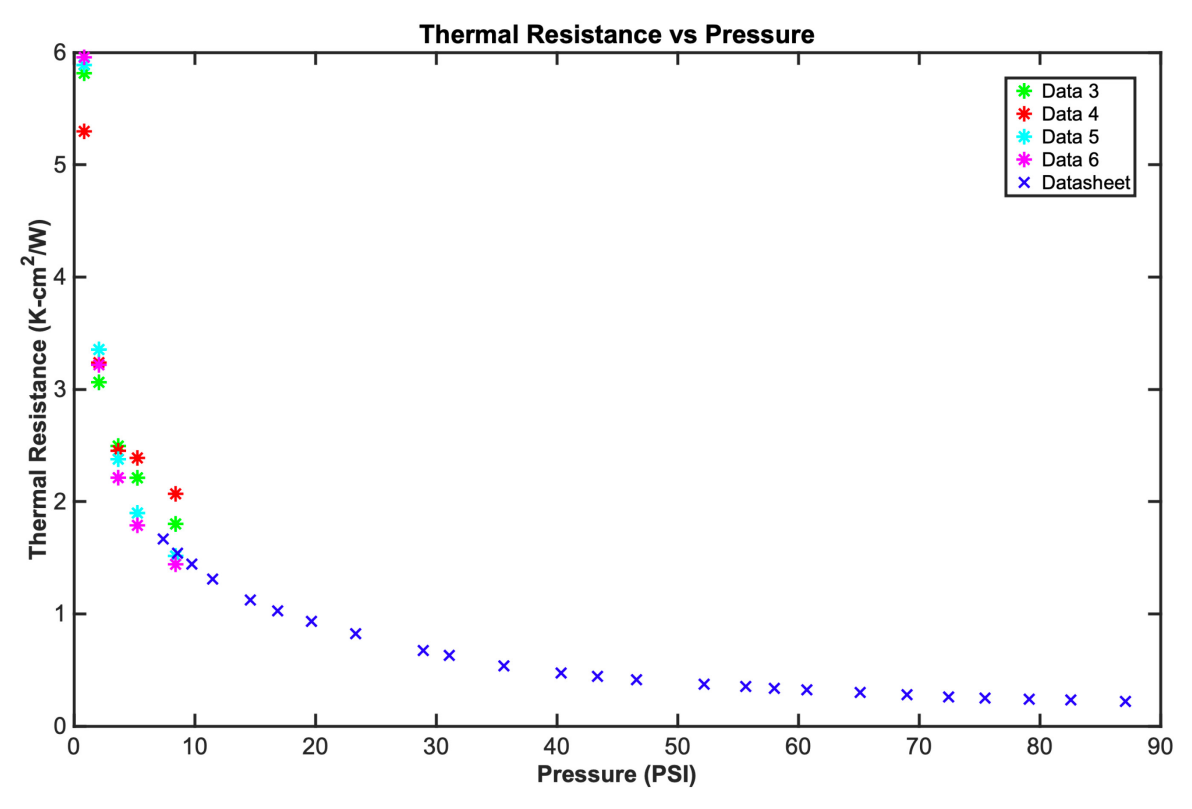


Fig. 11. Plot showing completed thermal resistance vs pressure curve that integrates data taken from the Panasonic PGS data sheet (blue data) and the raw thermal resistance data collected with the TIM Tester rig (colored data).

At each of the five pressures, the four resistance measurements were averaged to yield a final data point for the curve. The five points derived from these experiments are listed below.

Table 5. Corresponding pressures and average thermal resistances at said pressures from TIM Tester experiments

PRESSURE (PSI)	Average Thermal Resistance	Standard Deviation (K/W)
	(K/W)	
0.8493	5.739	0.3004
2.0656	3.218	0.1202
3.6677	2.384	0.1240
5.2535	2.072	0.2771
8.4239	1.707	0.2871

Graphically the average thermal resistances can be seen below. In this case the average thermal resistances that were derived from the experiments conducted in this thesis are colored magenta while those taken from the data sheet of the PGS used are in blue.

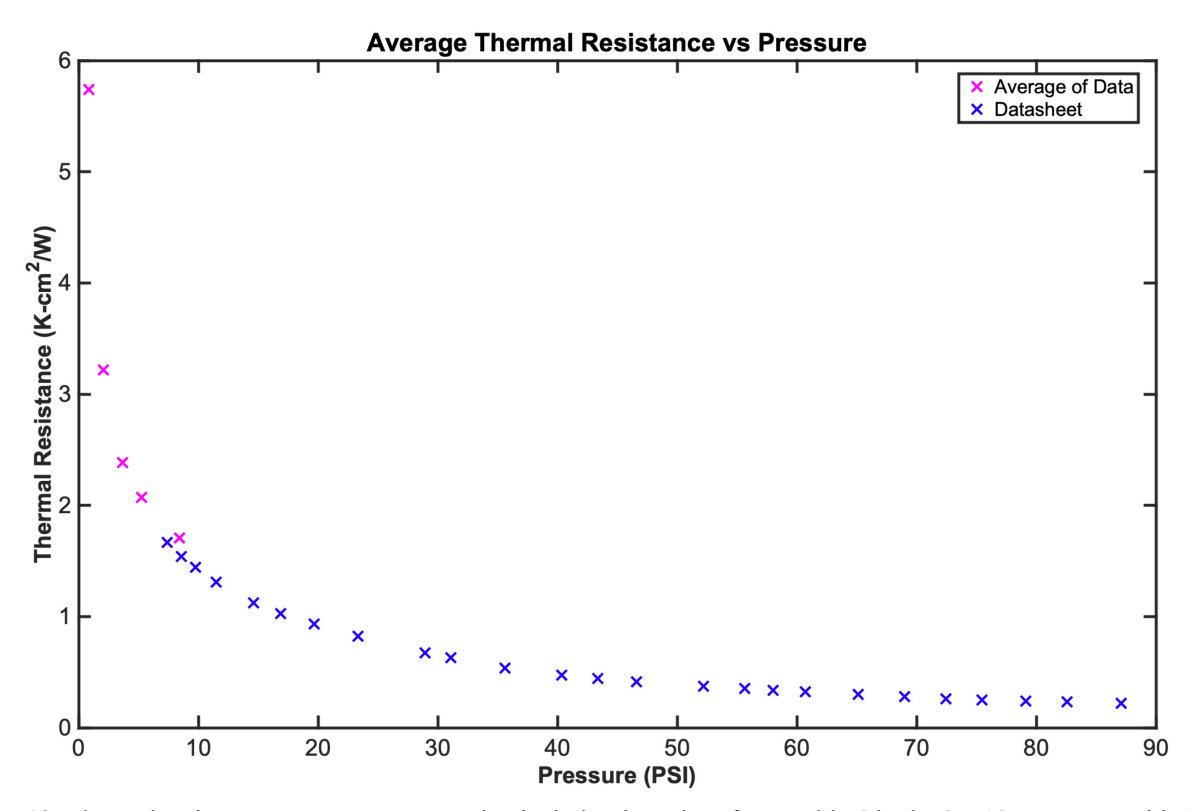


Fig. 12. Thermal resistance vs. pressure curve that includes the values from Table 4 in the 0-10 PSI range with the values extracted from the Panasonic PGS datasheet. [10]

4.4 Discussion

These resistance values are useful in gaining a physical intuition for the thermal performance of PGS, especially when thinking about the high vs. low pressure values; however, thermal resistance is not a value that is typically useful when making predictions for overall system behavior, notably with computational or simulation methods. Typically, thermal conductivity is the input used to inform these simulations that make system thermal predictions. To yield thermal conductivity as a function of pressure, first the relationship between thermal resistance and thermal conductivity must be established such that

$$R_{TH} = \frac{L(P)}{kA} \tag{5}$$

where k is thermal conductivity, R_{TH} is thermal resistance, A is the cross-sectional area associated with an interface, and L(P) is the thickness of the element, in this case PGS, as a function of the interface pressure. When rearranged to yield thermal conductivity as an output the equation becomes

$$k = \frac{L(P)}{AR_{TH}} \tag{6}$$

To acquire the values in equation 6, A is a measured dimension of the cross-sectional area of the aluminum cylinder, and R_{TH} is found from the curve produced by the combination of the PGS datasheet and the data measured by the TIM Tester rig. For the pressure-dependent thickness, the thickness can be derived from the compressibility curve of the PGS in the datasheet, using the blue curve for EYGS 200 μ m.

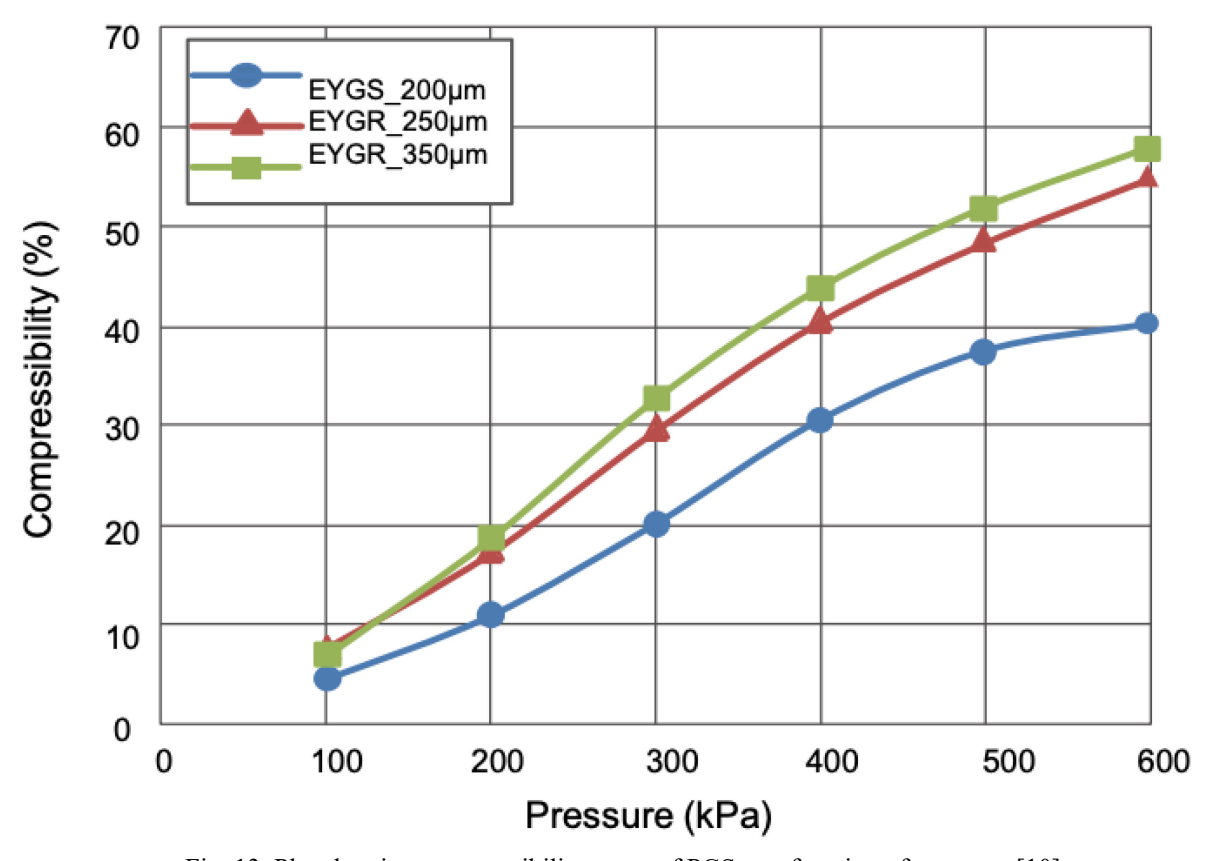


Fig. 13. Plot showing compressibility curve of PGS as a function of pressure. [10]

This curve, seen above in blue, gives the percentage of compression as a function of the interface pressure. When the percentage is converted into its decimal form, by multiplying by 0.01, and then subtracted from one, the resulting value is something that will be referred to as the compression factor. This operation can be seen in

$$F_{comp}(P) = 1 - 0.01C_{\%}(P)$$
 (7)

Once this factor is obtained, $F_{comp}(P)$ is then multiplied by the original thickness of the PGS sheet, L_{orig} , yielding the thickness of the PGS sheet as a function of pressure. This operation is detailed in

$$L(P) = L_{orig} * F_{comp}(P)$$
 (8)

Once the blue curve in the PGS compressibility curve is adjusted using these two operations, a curve can be extrapolated to pressures from 0-100 PSI. This was done by fitting a third order polynomial model to the resulting thickness data. The resulting curve can be seen below.

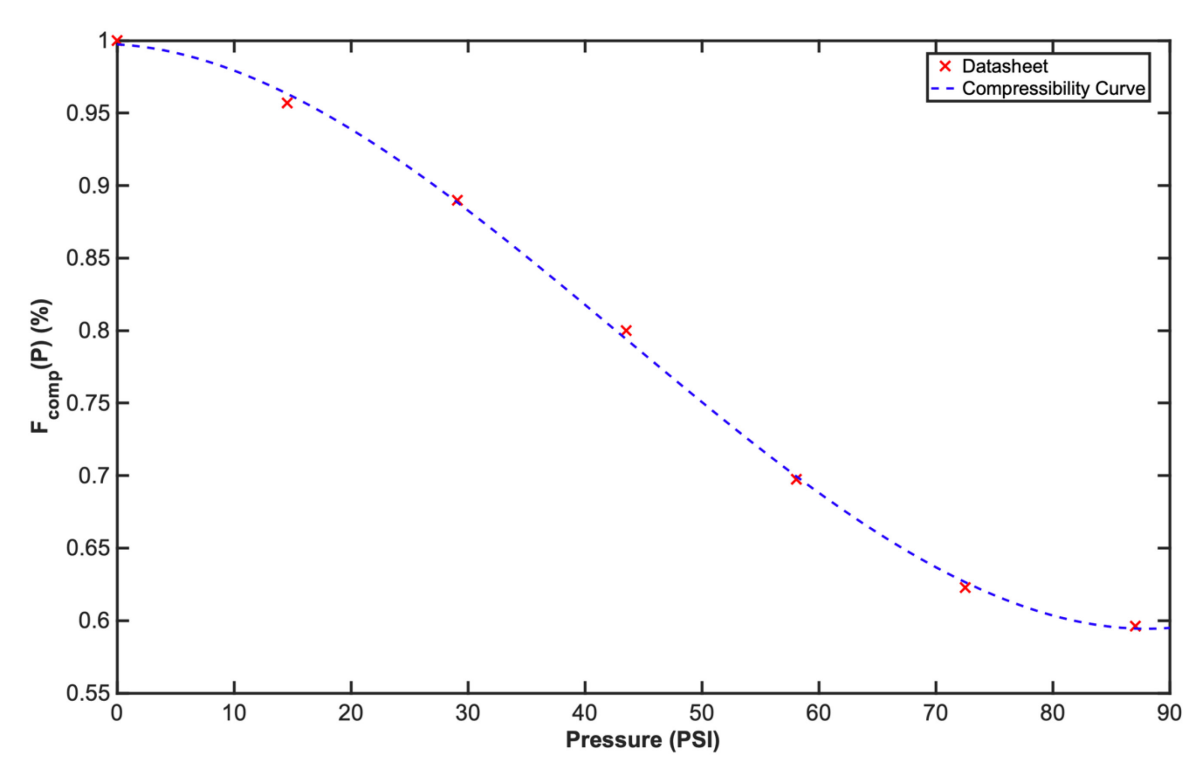


Fig. 14. Plot showing derived compression factor vs pressure curve that would be used to derive thermal conductivity of PGS as a function of pressure.

By obtaining a final curve that outputs PGS thickness as a function of interface pressure, the conductivity versus pressure curve can be derived for 0.2 mm thick PGS. This can be done by combining the function describing L(P) and the thermal resistance values that were gathered experimentally into the conductivity equation given above. When the gathered resistance data is filtered into the compression factor and conductivity relation, the conductivity versus pressure curve is derived for PGS between 0-100 PSI. The figure below shows this curve only through 40 PSI. This is because for the iPEBB use case the ESRDC is anticipating that interface pressures any higher than this would require a structural design complexity that would warrant shifts from the dry interface liquid cooling concept.

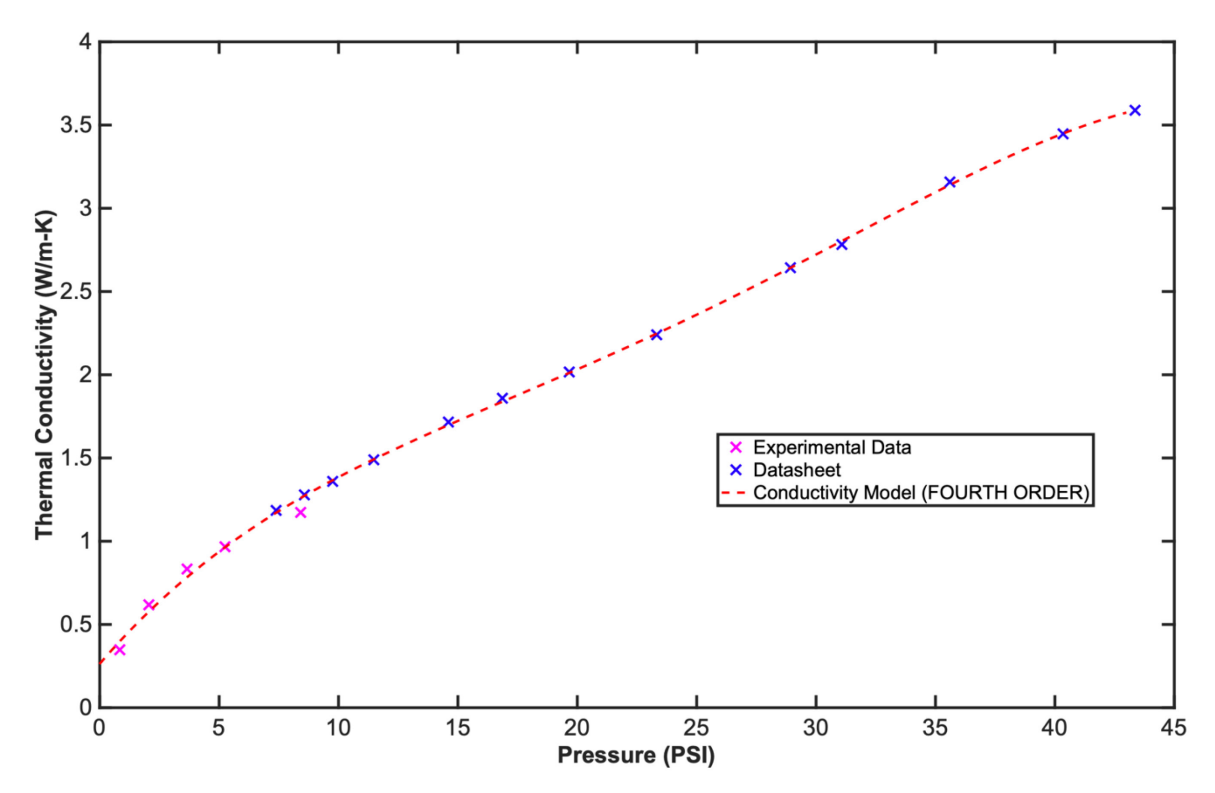


Fig. 15. Thermal conductivity vs pressure curve (red) derived from the data points seen in magenta and blue.

The magenta points illustrate the conductivity data that was obtained via the TIM Tester rig while the blue points indicate the data taken from the PGS datasheet. This data was then fit with a fourth order polynomial fit of the form

$$k_{fit}(P) = c_1 P^4 + c_2 P^3 + c_3 P^2 + c_4 P + c_5 \tag{9}$$

where the constants c_n are given below.

Table 6. List of polynomial constants for fourth order conductivity model of PGS

Polynomial Constant	Value
c_1	-2.257e-06
c_2	0.0002216
c_3	-0.007441
C4	0.1667
<i>c</i> ₅	0.261

This fourth-order model has an R-square value of 0.9988, and the coefficients were derived using 95% confidence bounds. The derived function $k_{fit}(P)$ thus can give conductivity predictions for PGS at any interface pressure between 0-40 PSI.

The fourth-order conductivity model generated by the TIM Tester rig is crucial because of its potential application in numerical modeling and simulations. The data taken in the 0-10~PSI range is followed quite continuously by the data from the 0.2~mm thick PGS data sheet.

Chapter 5 Pressure Proximity Rig

5.1 Design

While the TIM Tester rig was designed to explore the 1-dimensional thermal behavior of PGS, a different rig was used to explore how pressure magnitude and profile shape affect the performance of the PGS on a heat load of shape similar to that of the iPEBB. This rig was designed such that two-dimensional pressure measurements and temperature measurements could be taken simultaneously without interfering with the thermal path between the resistor heated plate, which emulates the casing of the iPEBB, and the cold plate. To ensure no interruptions in the thermal path, the rig was symmetric about the midplane of the cold plate. This allows two identical interfaces to be created on either side of the cold plate: one for the pressure measurement and one for the heat transfer path. This symmetry allows the argument for pressure profile congruency between the two surfaces of the cold plate to be made, meaning that both interface pressure profiles and heating element temperatures could be recorded simultaneously. The pressure congruency argument does not take into account the differences in surface finish and manufacturing tolerances between the plates. This issue became more apparent when the repeatability of the rig's pressure and temperature performance were experimentally determined.

Specifically, the pressure proximity rig design, depicted in Figs. 3 and 4, contains four 1.5" x 1" resistors supplying heat to a 6" x 6" x 0.25" aluminum plate. The PGS is placed between this heated aluminum plate and the cold plate. This puts the PGS in the critical thermal interface between the first aluminum plate, which the resistors are attached to, and the cold plate, which supplies the cooling via chilled water to the system. The cold plate is the ATS-TCP-1021, which has 6 total passes of fluid through its stainless steel 0.5" ID piping. The dimensions of the ATS cold plate are 152mm x 119mm x 15mm with a total of 229 mm of piping for the coolant.

The pressure sensor is placed on the side of the cold plate furthest from the resistors. Atop the pressure sensor a second aluminum plate, identical to the first plate at the bottom of the stack, is added. Again, this places the pressure sensor at a position symmetric to the PGS about the midplane of the cold plate. This means that when a pressure load is applied, the PGS should experience the same pressure profile as the pressure sensor allowing us to draw the pressure congruency arguments discussed earlier.

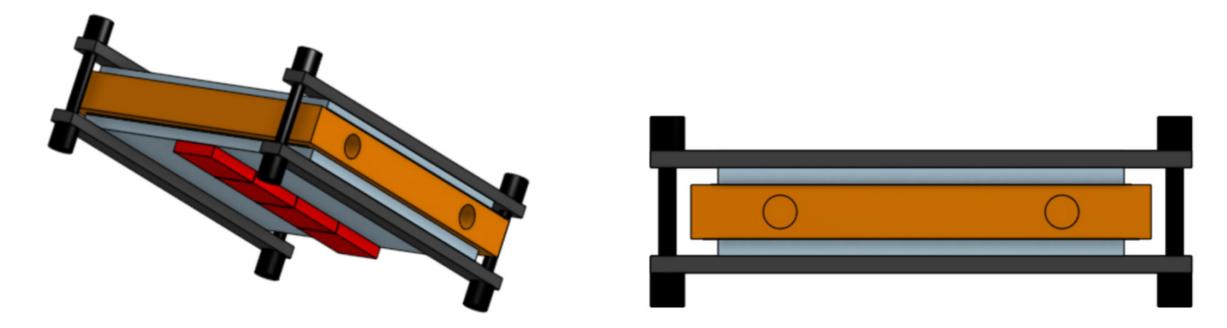


Fig. 16. CAD model of Pressure Proximity Rig

Pressure is applied to the stack via four 6-32 bolts. These bolts are passed through two sets of 12" x 0.5" x 0.5" steel braces, which ensure minimal bending deformation occurs in the aluminum plates; instead, the bending deformation is absorbed in the steel braces. The system contains ten total braces. Two each top and bottom on the far edges running parallel to the piping of the cold plate, and six running orthogonal to the original parallel supports, passing between the resistors. Due to the symmetry of the rig, the pressure experienced by the PGS is the same as the pressure experienced by the pressure sensor when the bolts are torqued.

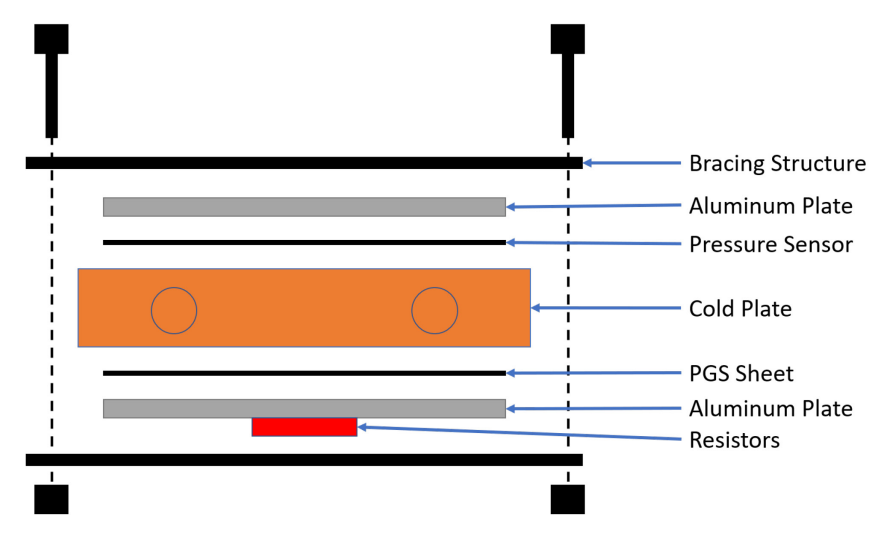


Fig. 17. Pressure Proximity Rig Exploded View

The full experimental rig can be seen in Fig. 18. The resistors are on the surface facing the camera, and the pressure sensor can be seen with green edges extending out to the left of the rig.

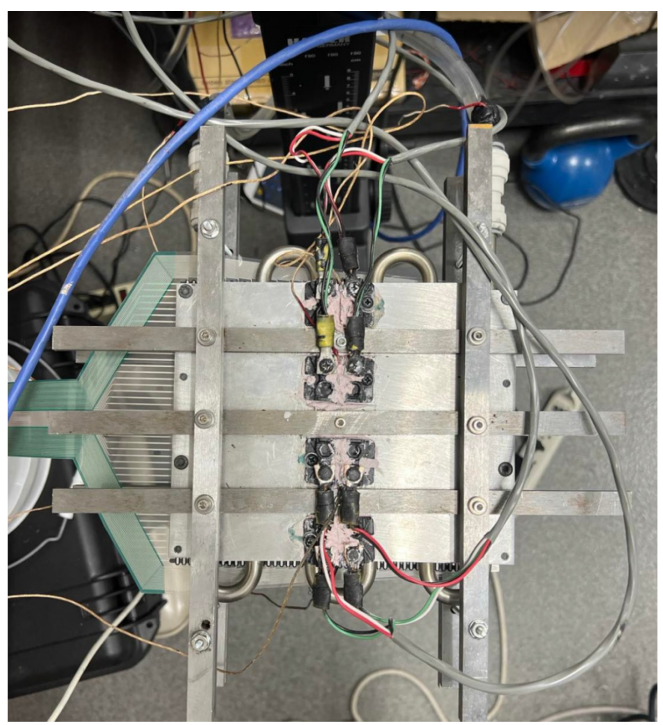


Fig. 18. Pressure Proximity Rig with cross bars and supports.

The results obtained by using this experimental setup are subject to both controllable and uncontrollable factors that may impact the data. The factors that are controllable include the pressure exerted on the system, the inlet temperature of the cooling water, the heating load of the heating elements, and the flow rate of the water. Factors that are not in the control of the setup include the ambient air temperature, the view factors associated with radiative heat transfer, and the manufacturing tolerances of the surfaces used in the pressure stack, specifically the top and bottom aluminum plates that are placed at the pressure and thermal interfaces and the faces of the cold plate. These factors must be considered and addressed when analyzing any data taken using the pressure proximity rig, and theoretical calculations and analytical models must be compared to the data to ensure some amount of congruency in the results.

5.1.1 Sensors

Within this rig, there were three types of sensors used: k-type thermocouples for sensing temperature, a Digiten flowrate sensor, and the Tekscan I-scan pressure mat. The associated ranges and uncertainties for these sensors are shown in Table 7. All sensors were calibrated before use. The pressure senor that is used is the Tekscan I-scan 5151 pressure mat [8]. This mat has an array of 44 by 44 sensor elements, each approximately 1mm square. The pressure sensors are first equilibrated, then calibrated. The sensors used in the experiments contained in this paper were taken to the Tekscan company headquarters in Massachusetts for equilibration. This process involves exerting a known uniform pressure on the sensor using specially designed rigs containing pressure bladders and compressed air, ensuring each of the cells report the same pressure. This equilibration was accomplished at a set 10 PSI for the sensors used in the pressure proximity rig. After the equilibration was completed, the calibration of the sensor was then conducted. The calibration was accomplished according to a multipoint calibration process discussed in depth in the I-scan manual [8]. The sensor was loaded with four different known masses. If the curve in the I-scan software between the measurements is confirmed to be linear, the process is successful and the calibration

can be applied to any measurements conducted using the sensor. In the case of the sensors used in the data collected with the pressure proximity rig, the resulting calibration process was successful.

Table 7. Sensors i	ised in PPR	with associated	uncertainties and ranges

Sensor	Manufacturer	Range	Uncertainty	Quantity
k-type thermocouples	Adafruit	-270 – 1372 C	2.2 C	7
Flowrate sensor	Digiten	1 – 30 LPM	Unknown	1
I-scan 5151 Pressure Mat	Tekscan	0 – 150 PSI	3% - 9%	1

5.2 Trials

Before conclusions can be made about the data taken using the pressure proximity rig, the repeatability of data produced by the rig must be established. The repeatability was determined by analyzing five different experiments with identical experimental settings. By holding the settings of the experiments constant, the repeatability of the rig could be determined by comparing the residuals of different pressure metrics and the resistor temperature data to the uncertainty associated with each of the sensors. The ambient conditions of the system were also recorded. The uncertainty in measurements using the Tekscan pressure sensor is 3% - 9% of the average pressure recorded on the interface of interest [6]. For the k-type thermocouples used to measure the temperature of the four resistors on the rig, the associated uncertainty is 2.2 C [7]. To determine the repeatability of the pressure proximity rig results, five experiments were conducted under identical thermal and compressive loads. More specifically, the four screws that apply the pressure onto the PGS and the Tekscan pressure sensor were all tightened to the same torque of 4.0 in-lbs. An example of the pressure data maps/profiles recorded by the Tekscan pressure sensors is shown in Fig. 19. The pressure data from these five experiments were compared via three different pressure metrics: average interface pressure, resistor pressure proximity value, and a cell-by-cell comparison. The average interface pressure, P_{avg} , is simply the mean of all values recorded by the pressure sensor

$$P_{avg} = \sum_{i=1}^{k} \left[\frac{P_i}{k} \right]$$
 (10)

where P_i is the pressure at the i^{th} cell on the pressure mat and k is the number of sensor elements, called sensels, in the pressure sensor being used. There are 1936 sensels arranged in a 44 by 44 grid in the sensor.

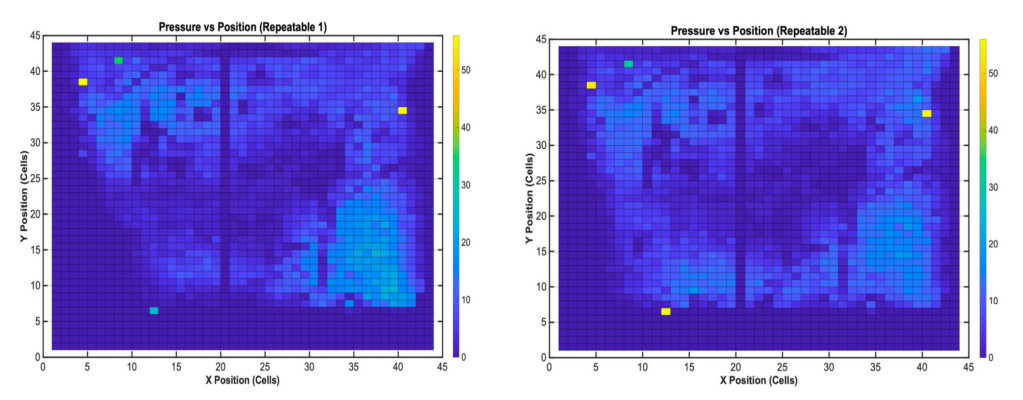


Fig. 19. Pressure profiles from two of the repeatability experiments with identical thermal and compressive loads.

The resistor proximity value, τ_n , was determined for each of the four resistors on the rig

$$\tau_n = \sum_{i=1}^k \frac{P_i}{d_{i,n} P_{avg}} \tag{11}$$

where $d_{i,n}$ is the distance to the i^{th} sensel from the n^{th} resistor and k is the number of sensels. The units of the proximity value, τ , are 1/distance due to the normalization by the average pressure of the interface. The proximity value of a given resistor is a measure of how much pressure is close to the resistor; a large value indicates pressure concentrated close to the resistor, and a small value indicates pressure concentrated away from the resistor. The final pressure metric is the cell-by-cell measurement recorded by the pressure sensor, P_i . In these experiments, not every sensel was loaded. Thus, only the loaded sensels were used in the analysis. For the cell-by-cell comparison, these values were compared directly to one another across experiments. Thus, each sensel value was compared to the identical sensel from each of the experiments. For the temperature metrics of repeatability, the values that were compared were the steady state temperatures of each of the four resistors on the rig. These steady state values were compared across the five experiments and thus allow for conclusions to be made regarding whether identical settings on the pressure rig result in the same resistor temperatures.

5.3 Average Pressure Results

As detailed above, the average pressure of the interface was determined using equation (10) for each cell located between the two plates. The average pressures and standard deviations for the five experiments can be seen in Fig. 20.

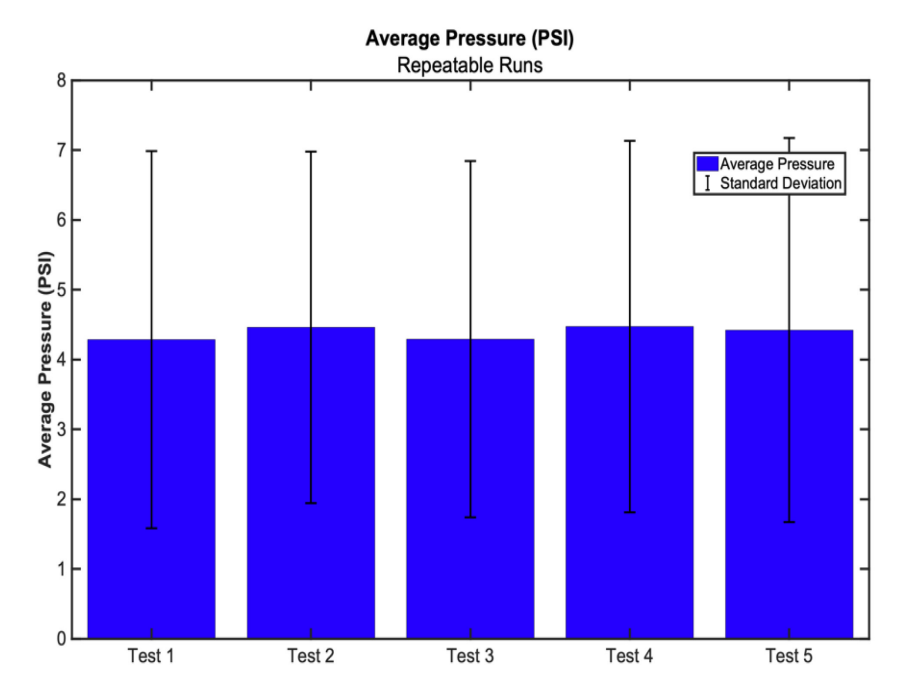


Fig. 20. Average pressure and standard deviations for five experiments to determine rig repeatability.

The mean average pressure across the five experiments, $\overline{P_{avg}}$, was 4.38 psi with a standard deviation of 0.0915 psi. The residual, R_P , of each experiment is

$$R_{P,m} = \frac{abs(P_{avg,m} - \overline{P_{avg}})}{\overline{P_{avg}}}$$
 (12)

where m is the experiment number. The mean residual of the average pressure,

$$R_{P,avg} = \frac{1}{5} \sum_{i=1}^{5} \frac{abs(P_{avg\cdot i} - \overline{P_{avg}})}{\overline{P_{avg}}}$$
 (13)

can be compared the uncertainty of the pressure sensor. The calculated value using the five average pressures is $R_{P,avg} = 0.018$ or 1.8%. This residual value is less than the uncertainty associated with the pressure sensor when recording average pressure, whose range is 3% - 9%. Therefore, the pressure profile rig produces repeatable average pressures across the interface of interest, when all of the experimental settings are held constant.

5.4 Proximity Value Data

To examine the proximity value repeatability, a similar process was used. First, the proximity values for each resistor, in each experiment, were calculated using (11). These values can be seen in Fig. 21. Next, the means and standard deviations for the proximity value of each resistor across the five experiments were calculated. These results can be seen in Fig. 22.

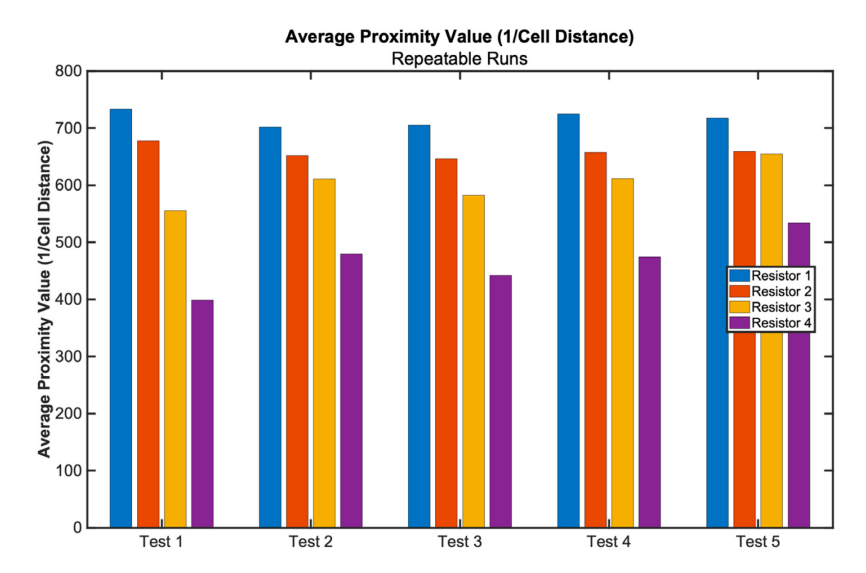


Fig. 21. Proximity values from four resistors in each of five experiments

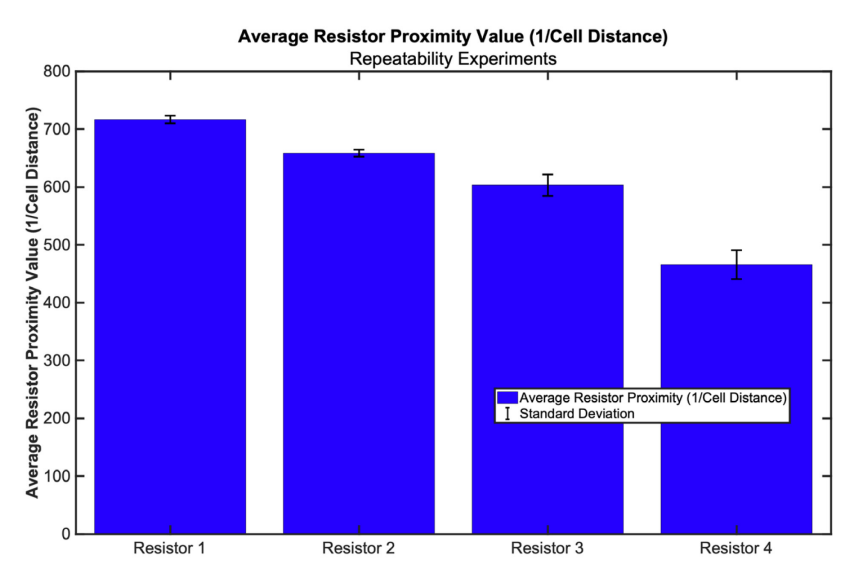


Fig. 22. Average proximity values for each of the four resistors across all five experiments.

The average proximity value residual value was determined using a process similar to the that used to calculate the residuals of the average pressure measurements. First, the average proximity values for each resistor were calculated across the five experiments. These values will be denoted as $\overline{\tau_{avg,n}}$, where n is the resistor for which the value is calculated. The proximity value residual $R_{\tau,n,m}$ for the n^{th} resistor in the m^{th} experiment is

$$R_{\tau,n,m} = \frac{abs(\tau_{avg,n,m} - \overline{\tau_{avg,n}})}{\overline{\tau_{avg,n}}}$$
 (14)

Each of these 20 residual values were then averaged across the five experiments. This yielded a mean average proximity value residual of 0.0375, or 3.75%. The residual calculated is within the lower end of the uncertainty range of 3% - 9% for the sensor. Thus, the pressure proximity rig is able to repeatably produce resistor proximity values across the interface of interest, when all of the experimental settings are identical.

5.5 Cell to Cell Data Across Experiments

The last metric used to check the repeatability of the pressure profiles compares the exact profiles from each experiment to one another. This means each cell was compared to the identical cell across all five repeatability experiments. To determine an average profile, S_{avg} , the five profiles were averaged

$$S_{avg} = \frac{1}{m} \sum_{j=1}^{m} P_j \tag{15}$$

where m is the number of experiments. Thus, S_{avg} is a matrix of the same size as P. This average profile is then used to calculate the residuals of each cell for each of the five experiments, where

$$R_{S,avg} = \frac{1}{k} \sum_{i=1}^{k} \frac{abs(P_i - S_{avg,i})}{S_{avg,i}}$$
 (16)

with a resultant value that indicates the average residual value of the k cells on the Tekscan pressure mat for each experiment. These values are plotted in Fig. 23. The average residual across all five experiments is

$$\overline{R_{S,avg}} = 0.2727 \sim 27\%$$
 (17)

which is much higher than the 9% maximum uncertainty value detailed above. Thus, the pressure proximity rig cannot produce repeatable pressure profiles on a cell-by-cell basis across the interface of interest, when all of the experimental settings are identical. This may be due to slight changes in the position of the pressure mat relative to the surface finish of the plates.

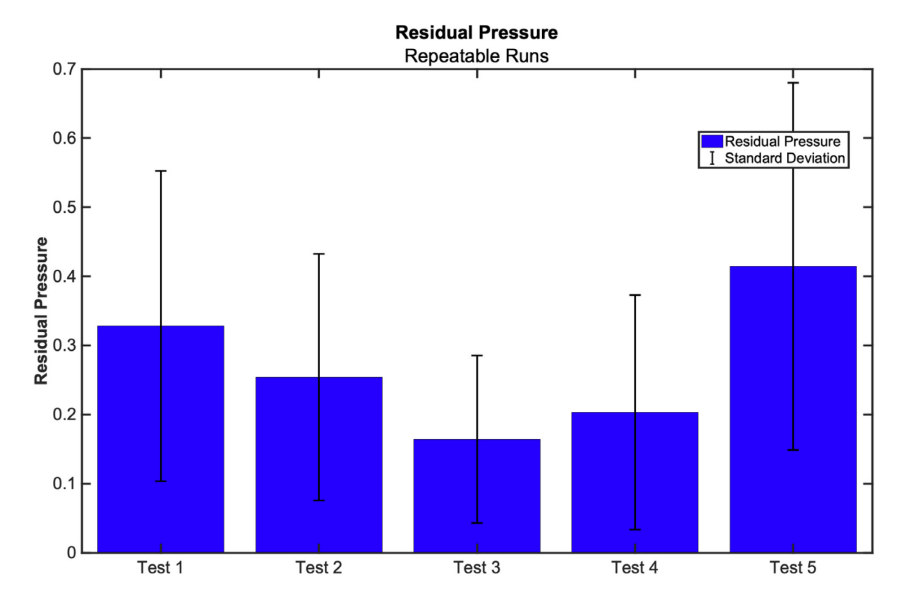


Fig. 23. Average profile residuals for each experiment.

These results and analysis indicate that the rig can produce repeatable profiles when characterized by average pressure and resistor proximity value, but cannot produce repeatable profiles on a cell-by-cell basis. As can be seen in the next section cell-by-cell repeatability is not required to produce repeatable resistor temperature results.

5.6 Corresponding Temperature Data

Now that the pressure metrics have been worked through, the next step to determining the repeatability of the proximity pressure rig is to look at the temperature metrics. The temperature metrics used to determine this were the four steady state resistor temperatures, the ambient air temperature, and the inlet water temperature. These temperatures were recorded using four k-type thermocouples with uncertainties of 2.2 degrees Celsius.

While assessing the four resistor temperature metrics it is important to keep in mind the assumption that the inlet water temperature to the cold plate and the ambient temperature (which can both be referred to as the fluid temperatures) were identical in the five tests for repeatability. The inlet and ambient temperatures were tracked using the same k-type thermocouples as the resistor temperatures. For the fluid temperatures to be determined as repeatable across experiments, the standard deviation of the five measurements for the ambient and inlet fluid temperatures must be smaller than the uncertainty of the sensor, 2.2 C. For the inlet water temperature, the mean and standard deviation across the five repeatability experiments were 29.4 C \pm 0.2 C. For the ambient air temperature, the mean and standard deviation were 31.6 C \pm 0.4 C. The standard deviations of these measurements were both smaller than the thermocouple uncertainty, meaning the data collected in the five repeatability experiments was collected under identical thermal conditions.

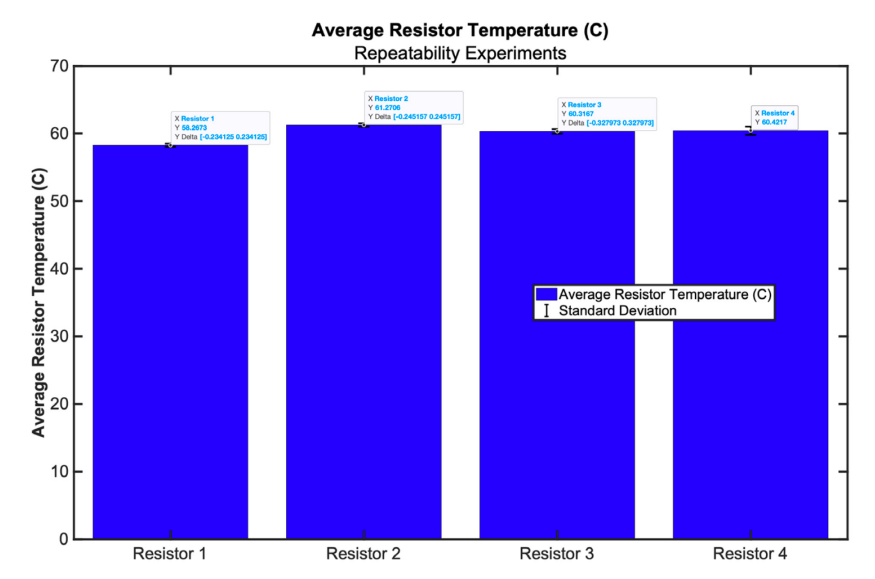


Fig. 24. Average steady state resistor temperatures across the five repeatability experiments.

To determine whether the resistor temperature results collected were repeatable, the data from each resistor across the five experiments was averaged on a resistor-by-resistor basis;

$$T_{avg,n} = \sum_{i=1}^{m} T_{n,i} \tag{18}$$

where n is the resistor number and m is the number of experiments. The residuals for the temperature values are calculated as

$$R_{T,n,m} = abs(T_{actual,n,m} - T_{avg,n})$$
 (19)

These residuals are then averaged as an aggregate. The mean average residual resistor temperature is $0.5C\pm0.3$ C. This residual value is less than the uncertainty associated with the k-type thermocouples used for measurement. This means that, under identical experimental settings, the resistor temperatures are reproducible.

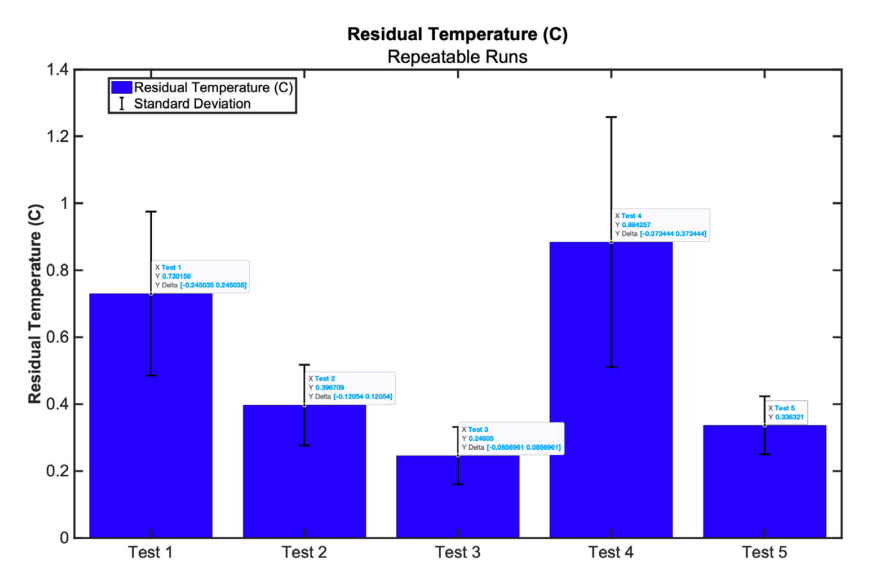


Fig. 25. The average residuals of resistor temperature for each experiment.

Consequently, from the five identical experiments conducted to determine the repeatability of the pressure proximity rig, it was determined that resistor temperature, resistor proximity value, and average interface pressure are reproducible, while the exact pressure profile, on a sensel-by-sensel basis, is not reproducible. Note that the resistor temperatures are well within the uncertainty bounds of the sensors. The fact that the temperature data is repeatable with residuals well within the uncertainty bounds of the sensors indicates that cell-to-cell repeatability in pressure measurements is not necessary to achieve repeatable results.

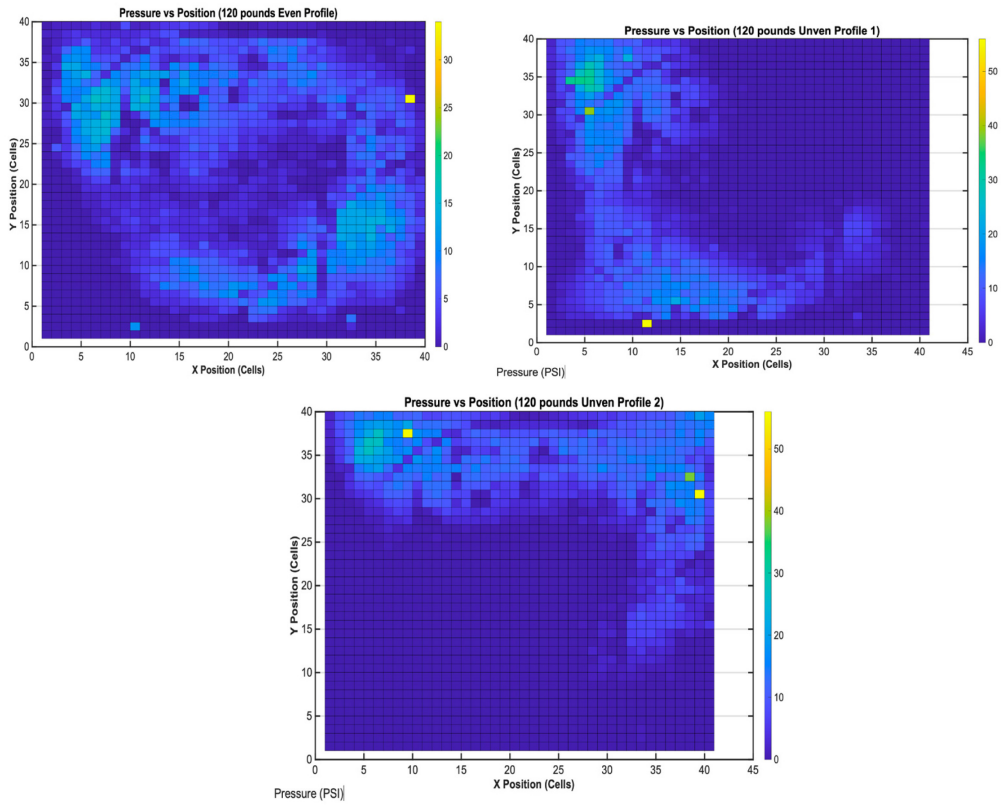


Fig. 26. Pressure profiles created using the pressure proximity rig showing even pressure across the full surface (top image), pressure concentrated along the left side of the rig (middle image), and pressure concentrated across the top of the rig (bottom image).

5.6.1 Results

The goal of the pressure proximity rig is to create varied pressure profiles across the surface in a controlled manner, then quantify the impact of the varied profiles on the performance of the thermal interface material. Three sample pressure profiles can be seen in Fig. 26, in which the top image shows an even profile, the middle image shows pressure concentrated along the left side of the plate, and the bottom image shows pressure concentrated along the top edge of the plate.

A set of experiments was run with a pre-planned arrangement of pressure profiles and overall average pressures. One example run is shown in Fig. 27. Resistors are numbered from right to left. It is evident from the pressure profile that pressure is concentrated on the left-had side of the surface; thus resistor R4 has a much higher pressure proximity value than resistor R1. The resistor temperatures for this run display a clear inverse correlation between pressure proximity value and temperature, displayed in the plot at the bottom of Fig. 27.

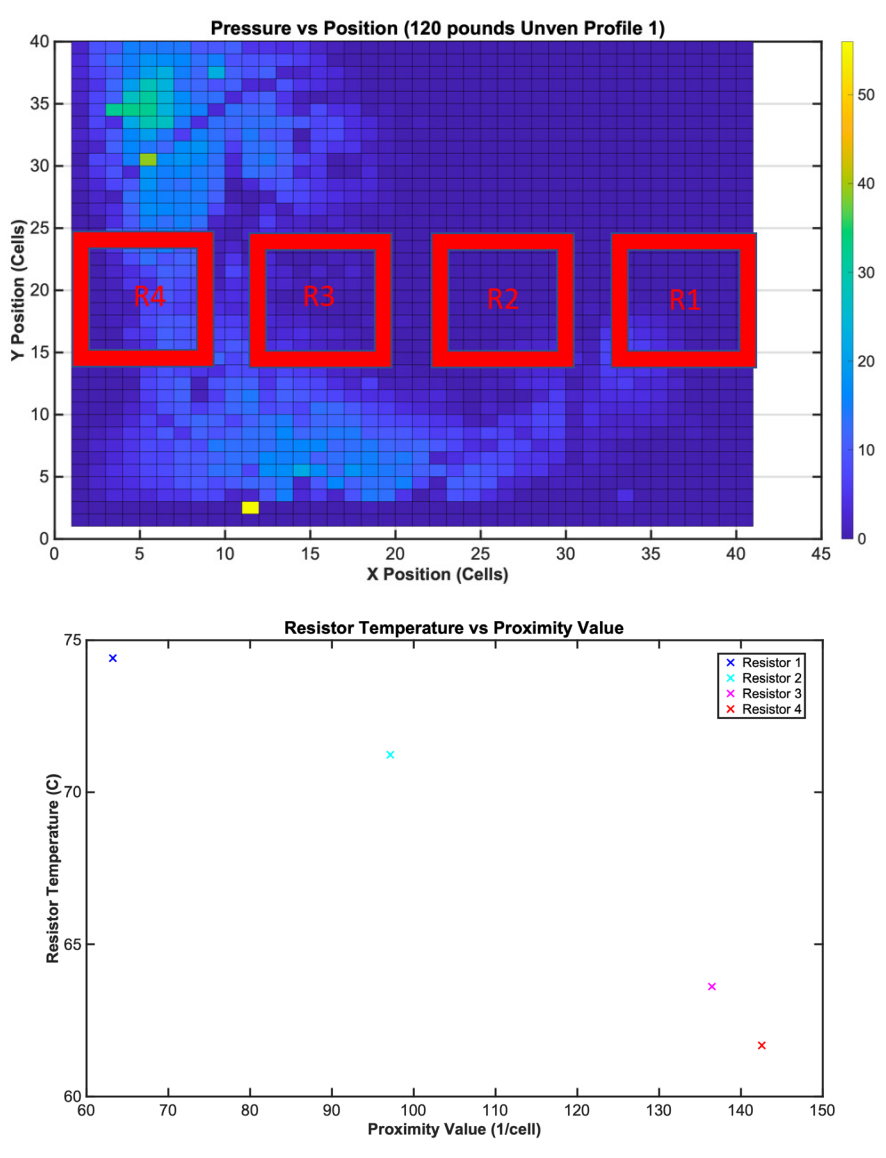


Fig. 27. Pressure profile and individual resistor temperatures for a single experiment, showing inverse correlation between pressure proximity value and temperature.

A comparison of resistor temperatures at various average pressures is shown in Fig. 28. This plot shows a strong inverse correlation between average pressure across the full plane and resistor temperature. Variations in temperature at similar average pressures are due to variations in pressure profile.

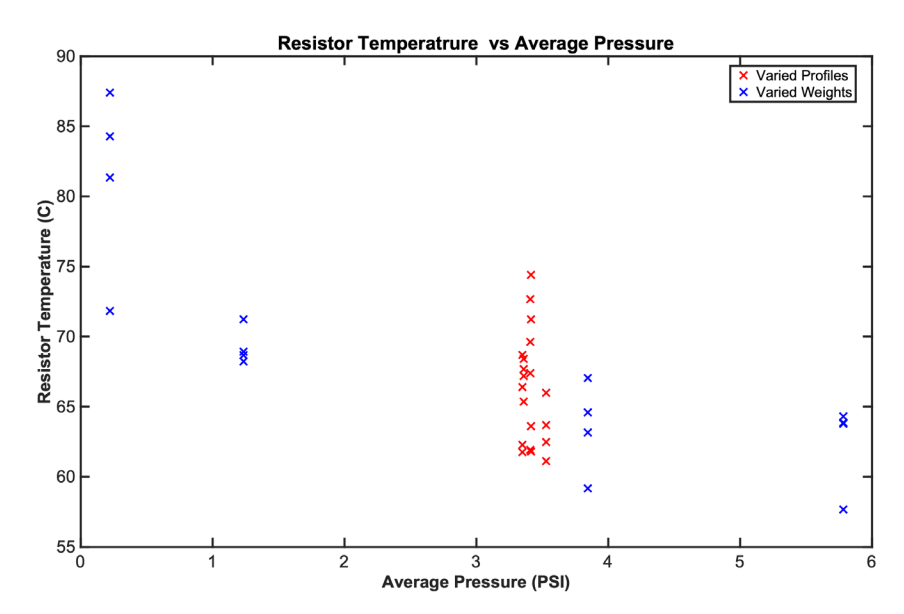


Fig. 28. Individual resistor temperatures plotted versus average pressure across the full plane for 21 individual experiments.

5.7 Empirical Model Development

The next step in this research was to formulate an empirically derived predictive model for the resistor temperatures based on the controllable pressure metrics. The model will be a linear least squares model of the form

$$T_{n,predict} = C_0 + C_1 P_{avg} + C_2 \tau_n \tag{20}$$

with two independent variables: interface average pressure, P_{avg} , and resistor proximity value, τ_n . The dependent variables in this case are the steady state temperatures of each of the four resistors on the rig. Thus, using the average pressure value and the resistor proximity value, the model should meaningfully predict the steady state temperature of any individual resistor.

The data used to develop this model was generated in eleven random experiments in which the average pressure and profile shapes were not specified but instead the rig's pressure creating screws were tightened to random torques creating random profile shapes. These 11 experiments were all conducted under the same thermal settings such that ambient temperature, water temperature, water flowrate, etc., were consistent throughout. Using the Matlab integrated least squares solver produced the coefficients shown in (21).

$$T_{n,predict} = 77.4262 - 2.4404 P_{avg} - 0.0379 \tau_n$$
 (21)

indicating a negative correlation between resistor temperature and the two independent variables, P_{avg} , and τ_n , which intuitively makes sense. The higher the average pressure, the lower the temperature should be. Likewise, the closer the pressure is to the resistor of interest, the lower the temperature of that resistor should be.

5.8 Accuracy of the Empirical Model

To gauge how good the model was in predicting resistor temperature from P_{avg} , and τ_n , 10 more experiments were conducted. These experiments were again in the same 0-6 PSI range. These 10 experiments supply 40 resistor temperature data points for comparison to the predictive model.

To make this comparison, first the data was collected and processed into, τ_n , P_{avg} , and $T_{n,actual}$. The pressure data, P_{avg} and τ_n , for each of the resistor data points (40 in this set of experiments), was then used in (21) to derive 40 resistor temperature predictions, $T_{n,predict}$. The predicted temperatures were then compared to the actual temperatures. Residuals were calculated in two ways: with a percentage comparison, R_{deg} , and a degree comparison, R_{deg} , where

$$R_{\%} = 100 \frac{\sqrt{(T_{n,actual} - T_{n,predict})^2}}{T_{n,actual}}$$
 (22)

and

$$R_{deg} = \sqrt{(T_{n,actual} - T_{n,predict})^2}$$
 (23)

The result was 40 values for each of these residual calculations. The average residuals between the predictive model and the actual temperatures, with the same P_{avg} , and τ_n , are 2.5C \pm 2.0C for the degree comparison, and 3.7% \pm 2.9% for the percentage comparison. This means that the predictive model can predict the resistor temperature on the pressure proximity rig within 2.5C \pm 2.0C, with only the average pressure on the thermal interface P_{avg} , and the proximity value for that resistor, τ_n .

To visualize the prediction space related to the actual temperature values from the 40 experiments, Fig. 29 shows these comparisons. Note that maximum error is less than 7 C. Fig. 29 shows how the predicted values compare to the 40 actual temperature values. The predicted space is of all of the possible resistor temperatures from the ranges of P_{avg} , and τ_n , that are within the axis ranges.

The results of these experiments provide a thorough empirical analysis of how to predict heating element temperature from known pressure metrics of average interface pressure and proximity value.

5.8.1 Discussion

The empirically derived linear least-squares model has an accuracy of $2.5C \pm 2.0C$. This accuracy is quite high considering the uncertainty of the thermocouples used to collect the temperature data is 2.2 C. The derivation of this model, using the experimental design that leverages average pressure and proximity value as independent variables can be replicated on any flat system

that might require a TIM paired with an interface pressure to ensure good heat transfer. What the results of the model show, is that pairing the Tekscan I-scan pressure sensor with thermocouples monitoring component steady state temperatures to produce a linear least squares model, produces a model that can predict component temperatures within 4% of the actual system thermal behavior.

From the predictive temperature model in (21), the coefficients associated with the two independent variables reveal what factors dominate component temperature. The magnitude of the constant associated with the average pressure of the interface is over 64 times larger than the magnitude of the constant associated with the proximity value. This simple analysis and comparison indicate how average interface pressure affects the final component temperature much more than the components proximity value on the pressure proximity rig.

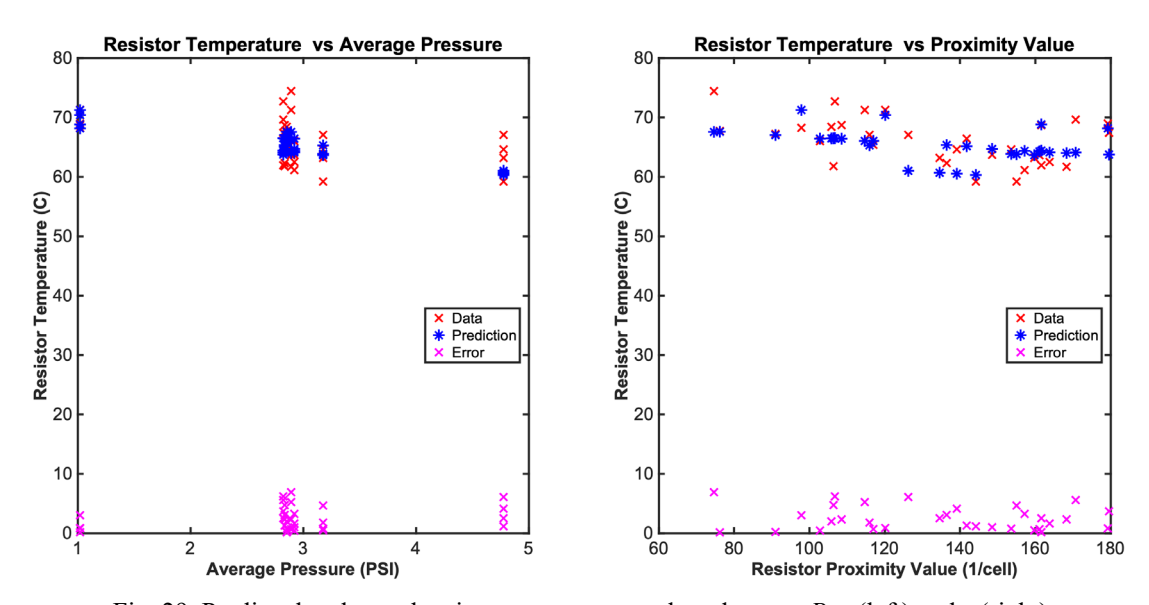


Fig. 29. Predicted and actual resistor temperatures plotted versus P_{avg} (left) and τ (right).

The empirical model that was derived, and its presented accuracy, indicate how important understanding how pressure will be applied to the iPEBB cold plate interface. Understanding what this pressure profile will look and pairing this understanding with live thermal testing in a similar manner to what was conducted for the pressure proximity rig will give the ESRDC the data needed to be able to predict iPEBB thermal performance from interface pressure profiles.

Chapter 6 CFD Simulation

One common technique to verify any thermal modeling, whether that be empirical or analytical analysis, is Computational Fluid Dynamics (CFD) simulations. CFD simulations are useful because they allow for comprehensive three-dimensional visualizations of systems under load cases that theoretical analysis cannot supply, while also being faster than empirical modeling. Despite this, it is important to understand that simulations are only as good as their set-up. Thus, it is crucial that exact initial and boundary conditions are set so that the simulation can solve the correct load cases. It is also incredibly important that the bodies being analyzed have the correct material properties such as thermal conductivity and specific heat, to ensure an accurate result. In the simulations presented in this section, a standard tetrahedral mesh was used to model four of the experiments run with the Pressure Proximity Rig. The experiments that were simulated, from the Pressure Proximity Rig, include four pressure profiles in which the four bolts that apply the interface pressure to the stack were all tightened to the same torque. While this did not necessarily ensure a completely uniform profile due to surface imperfections and deformation during loading, the resulting profile could be approximated as such.

6.1 Design

As discussed, four simulations were conducted for four different pressure profiles. These four profiles were all approximated to be uniform, all with different average pressures across their interfaces. As determined in the experiments using the TIM Tester rig, different interface pressures will result in unique interface or contact thermal resistances for the PGS. In the CFD simulation, this change in PGS thermal resistance was modeled by adjusting the material properties of the PGS body in the simulation. The specific heat of the PGS was held constant, while the thermal conductivity was adjusted according to the fourth order polynomial thermal conductivity vs interface pressure model developed using the TIM Tester rig.

The properties and setting used in each of the four simulations were all different and set according to the parameters and conditions of the experiments from the PPR experiments. The parameters of the simulations can be split into three different categories: Fluid properties, PGS properties, and solid properties. The fluid properties are derived from the experimental data, specifically the Inlet water temperature of the cold plate and the ambient temperature of the air. The PGS properties are derived from the average interface pressure recorded in each experiment, which yields different thermal conductivity values for the PGS based on the fourth order model developed in the TIM Tester experiments. The solid properties are for the other bodies that were a part of the PPR. These bodies include the cold plate, the aluminum plate, the thermal paste between the resistors and heated aluminum plate, and the resistors used as heating elements. The resistors were the only of these three bodies which did not include critical material properties in

its data sheet. After further investigation, it was concluded that the resistor could be effectively modeled with two materials. The base of the resistor could be modeled as an aluminum baseplate, while the actual heating element of the resistor would be modeled as an appropriate thickness plate of Palladium Silver, [14] a common resistive material used in thick film resistors such as the Ohmite resistor used in the PPR. [15]

The fluid and PGS properties can be seen in the first table below. For each experiment, there were different properties, and these properties are all reported below.

Table 8. Fluid and PGS properties in four reference experiments and simulations

Experiment Number	Average Interface Pressure (PSI)	PGS Thermal Conductivity (W/m-K)	PGS Specific Heat (J/kg-K)	Inlet Water Temperature (C)	Ambient Temperature (C)	Heat Load per Resistor (W)
1	1.24	0.4419	850 [16]	30.01	31.4	65
2	3.8	0.7847	850	29.9	31.4	65
3	4.3	0.84	850	29.4	31.5	65
4	5.78	0.99	850	30.2	31.6	65

Unlike the fluid and PGS properties, the solid properties remained constant. These properties can be found below.

Table 9. Solid body material properties used in simulations

Part	Part Material	Thermal Conductivity	Specific Heat
		(W/m-K)	(J/kg-K)
Cold Plate Body	Aluminum	235	897
Cold Plate Tubing	Steel	60	480
Heated Plate	Aluminum	235	897
Resistor Baseplate	Aluminum	235	897
Resistor Element	Palladium Silver	29 [17]	240 [17]
Thermal Paste	Silicone Gel	3.5	1000

These properties were all then input into the simulation software for the four different experiments.

Using the simulation settings and properties shown in the tables above, the simulations were conducted using a mesh with properties shown in the figure below.

Overall mesh quality:	0.151 (Acceptable range: 0.035 to 1.0)
This mesh meets our quality o	riteria.
Number of prisms:	140202
Number of volumes:	1195228
Number of faces:	2639669
Number of nodes:	349549
Number of pyramids:	25956
Number of quadrangles:	305841
Number of triangles:	2333828
Number of hexahedra:	27501
Run finished.	
Number of edges:	5507
Number of tetrahedra:	1001569
E' 20 M 1	1. 1

Fig. 30. Mesh quality and statistics (left) along with image of mesh applied to CAD of PPR.

6.1.1 Results

The simulations were all run until convergence. This convergence occurred at a different number of iterations depending on the simulation. Below, a figure shows the domain convergence plots for each of the four simulations. It is clear that all of the system properties being calculated converged with a special note on the temperature convergence which is seen by the light blue curve in the plots.

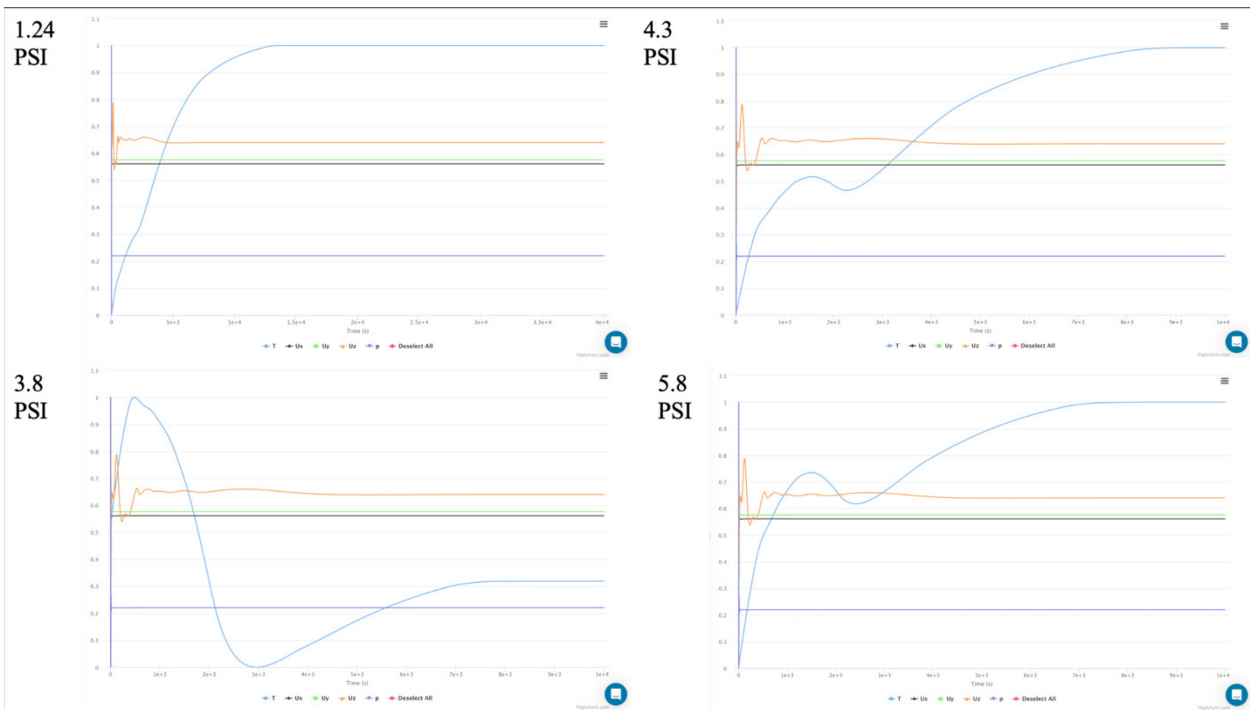


Fig. 31. Domain convergence plots for each of the four simulations run.

The convergence of each of these plots ensures that the temperatures that were output were in fact the steady state temperatures, thus meaningful comparisons can be made between the simulation results and the experimental data from the PPR.

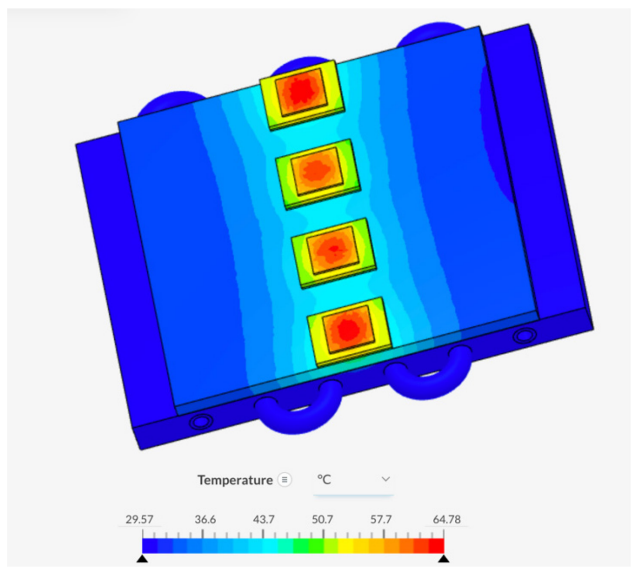


Fig. 32. Image of temperature solution field for 4.3 PSI simulation case.

The resistor temperature results of the four simulations can be seen in the table below. The specific data point that was recorded and used for comparisons is the average steady state temperature of the four resistors. This means the steady state temperature of each resistor was used to obtain a single average using the following equation,

$$T_R^{avg} = \frac{1}{4} * (T_{R1} + T_{R2} + T_{R3} + T_{R4})$$
 (24)

Table 10. Average resistor temperature results from each simulation

Experiment Number	Average Interface Pressure (PSI)	PGS Thermal Conductivity (W/m-K)	Inlet Water Temperature (C)	Ambient Temperature (C)	Average Predicted Resistor Temperature (C)
1	1.24	0.4419	30.0	31.4	69.2
2	3.8	0.7847	29.9	31.4	64.6
3	4.3	0.8348	29.7	32.1	63.9
4	5.78	0.99	30.2	31.6	63.5

The simulation results can be compared to the actual temperatures from the experiments. This comparison is important because the limitation of each the prediction method will be discussed enabling proper use in the future.

6.1.2 Discussion

First, the simulation results must be compared to the actual data from the PPR experiments. Below, the Average Predicted Resistor Temperature (from the simulations) are compared to the Average Actual Resistor Temperature from each experiment. These were both calculated using (24) with the resistor temperatures coming from the simulation and experiments respectively.

Table 11. Comparison of simulation results and reference experimental results

Experiment Number	Average Interface Pressure (PSI)	PGS Thermal Conductivity (W/m-K)	Average Predicted Resistor Temperature (C)	Average Actual Resistor Temperature (C)	Degrees Difference (C)	Percentage Difference (%)
1	1.24	0.4419	69.2	69.3	0.1	0.14
2	3.8	0.7847	64.6	63.5	1.1	1.7
3	4.3	0.8348	63.9	60.8	3.1	4.8
4	5.78	0.99	63.5	62.4	1.1	1.7

The average degrees difference between the simulation and the actual data is calculated to be $1.4C\pm1.3C$. The uncertainty associated with the k-type thermocouples used to measure the resistor temperatures is 2.2C. This means that the simulation prediction can predict the average resistor temperatures within sensor precision of 2.2 C. These results indicate that using the 4th order PGS conductivity model, developed using the TIM Tester rig, and integrating that model into CFD simulations is an effective method for predicting temperatures on systems like the PPR.

Chapter 7 Conclusions and Future Work

7.1 Conclusions

In this thesis, a critical component of the dry interface cooling solution, the thermal interface material between the cold plate and iPEBB, was investigated at depth. First, in Chapter 3, five commercially available TIMs were investigated for their thermal behavior at pressures less than 10 PSI as well as their structural qualities and usability metrics. This initial exploration was crucial due to the modular nature of the iPEBB and the human interaction that is necessary in its use.

In Chapter 4, a fourth order thermal conductivity model for PGS as a function of interface pressure was derived in the 0-10 PSI range. This model is incredibly important as it allows for future designers and researchers in the ESRDC to have conductivity inputs for the PGS in any thermal modeling done for future iterations of the iPEBB.

In Chapter 5, the design and testing of an experimental rig (PPR) for testing thermal interface materials under various average pressures and pressure profiles was presented. From the results of several experiments, an empirical model was developed that demonstrates the effect that interface pressure profile has on component temperatures with PGS as the acting TIM between the cooling solution and the heated system.

Finally, in Chapter 6, using the conductivity model developed in Chapter 4, CFD simulations of experiments conducted in Chapter 5 were run. These simulation results were then compared to the results of the PPR experiments and analyzed. Upon this analysis, it was discovered that using the conductivity model for PGS as an input in a CFD simulation is an effective way of modeling the contact resistance of PGS as a function of pressure. The effectiveness of the conductivity model – CFD simulation setup has a mean error of $1.4\text{C} \pm 1.3\text{C}$ between the simulation's outputted average resistor temperature and the actual average temperatures measured.

The experiments and simulations conducted in this thesis provide a blueprint for the necessary steps required to thermally model the iPEBB dry interface cooling system using CFD, as well as how to do so once a clamping mechanism for the iPEBB structure is designed.

7.2 Future Work

The iPEBB is a unique thermal problem because of the modularity with which it will be used. This modularity is the reason for exploration into the dry interface cooling design. This thesis has explored PGS at length as a viable TIM for this iPEBB's liquid cooled interface.

Despite this, it is crucial that the structural properties of PGS, the abilities of PGS to deal with grit in its interface, and how PGS performs when thermally cycled are explored in the future.

Two methods/tools have been built out in this thesis to explore and model the thermal behavior of PGS. First the conductivity vs pressure model of PGS was created. It was then demonstrated that this model could be used to accurately predict average component temperatures on a system with a heat load shape similar to that of an iPEBB. The next logical step would be to use this conductivity model in a full CFD simulation of the iPEBB. The interface pressure at the PGS interface could be altered until the MOSFET temperatures of the iPEBB are held to a desirable temperature.

These simulation results can then be used to inform the clamping system design of the iPEBB stack structure. With a known necessary effective conductivity of the PGS, an interface pressure can be solved for. With this pressure, the clamping mechanism can then be designed with actuators and mechanical properties that ensure the necessary interface pressure can be met reliably.

After the clamping system is designed, it can be prototyped, manufactured, and finally tested. This is where the Tekscan I-scan pressure system can be used. Much like in Chapter 5, upon the creation of this clamping system, the average pressure profile of the iPEBB – cold plate interface can be derived. The I-scan system is uniquely powerful because it gives a high-resolution pressure mapping of the entire interface. This will allow the ESRDC to make the best possible design decisions on how to tweak and iterate the clamping system design to ensure the best possible pressure profile for the PGS interface.

The process outlined above integrates the two methods created and used in this thesis, to design and finalize the dry interface cooling solution for the iPEBB.

References

- [1] "GE Powers US Navy's 1st Full-electric power and propulsion ship," *GE News*. [Online]. Available: https://www.ge.com/news/press-releases/ge-powers-us-navy%E2%80%99s-1st-full-electric-power-and-propulsion-ship. [Accessed: 26-Mar-2022].
- [2] C. Cooke, C. Chryssostomidis, and J. Chalfant, "Modular integrated power corridor," in *Electric Ship Technologies Symposium (ESTS)*, 2017 IEEE. IEEE, 2017, pp. 91–95.
- [3] T.Ericsen, N.Hoingorani, and Y.Khersonsky, "PEBB—power electronics building blocks from concept to reality," in *IEEE Petroleum and Chemical Industry Technical Conference 2006 (PCIC06)*. IEEE, September 11-13, 2006, paper PCIC-2006-22.
- [4] N. Rajagopal, "Design of 1.7 kV SiC MOSFET Switching Cells for Integrated Power Electronics Building Block (iPEBB)," Master's Thesis, Virginia Polytechnic Institute and State University, 2021.
- [5] "Pyrolytic graphite," Pyrolytic Graphite Thermal Interface Material | HPMS Graphite. [Online]. Available: https://hpmsgraphite.com/pyrolyticgraphitesheet?gclid=CjwKCAjwzeqVBhAoEiwAOrEmzRKAVonwnRXRT nOX4kR7lwJBfMpAkncuaX4MkVAwK6ueok-U812NyBoCrAwQAvD_BwE%29. [Accessed: 02-Mar-2023].
- [6] K. Bachus, A. Demarco, K. Judd, D. Horwitz, and D. Brodke. (2006). Measuring contact area, force, and pressure for bioengineering applications: Using Fuji Film and TekScan systems. *Medical Engineering & Physics*. 28. 483-488. 10.1016/j.medengphy.2005.07.022.
- [7] "Thermocouple," *Thermocouple accuracies Thermocouple Accuracy Thermocouple Accuracy Comparison Chart*. [Online]. Available: https://www.thermocoupleinfo.com/thermocouple-accuracies.htm. [Accessed: 02-Mar-2023].
- [8] Tekskan, Inc. *I-scan*TM & High Speed *I-scan User Manual*. South Boston, MA.2018.
- [9] Carlton, H., Pense, D., and Huitink, D., 2020, "Thermomechanical Degradation of Thermal Interface Materials: Accelerated Test Development and Reliability Analysis," Journal of Electronic Packaging, **142**(3), p. 031112.
- [10] "Eyg-S1516ZLSB: Digi-key electronics," *Digikey*. [Online]. Available: https://www.digikey.com/en/products/detail/panasonic-electronic-components/EYG-S1516ZLSB/6575949. [Accessed: 26-Apr-2023].
- [11] "Eyg-TF0F0A15A: Digi-Key Electronics," *Digikey*. [Online]. Available: https://www.digikey.com/en/products/detail/panasonic-electronic-components/EYG-TF0F0A15A/10479250. [Accessed: 26-Apr-2023].
- [12] "Tg-A126X-150-150-1.5: Digi-Key Electronics," *Digikey*. [Online]. Available: https://www.digikey.com/en/products/detail/t-global-technology/TG-A126X-150-150-1-5/7360875. [Accessed: 26-Apr-2023].
- [13] "Tg-APC93-150-150-1.5-0: Digi-key electronics," *Digikey*. [Online]. Available: https://www.digikey.com/en/products/detail/t-global-technology/TG-APC93-150-150-1-5-0/13246098. [Accessed: 26-Apr-2023].
- [14] "The Platinum Metals in Electronics," *technology.matthey.com*. [Online]. Available: https://technology.matthey.com/article/29/1/2-11/. [Accessed: 27-Apr-2023].
- [15] "TGHPVR500KE ohmite: Mouser," *Mouser Electronics*. [Online]. Available: https://www.mouser.com/ProductDetail/Ohmite/TGHPVR500KE?qs=5aG0NVq1C4x05U8Zw72fkQ%3D%3D. [Accessed: 27-Apr-2023].

- [16] "Thermal graphite sheets Mouser electronics," *Basic Properties and Application Examples of PGS Graphite Sheet*. [Online]. Available: https://www.mouser.com/pdfdocs/ThermalGraphiteSheets.pdf. [Accessed: 27-Apr-2023].
- [17] "Other metal alloy," *MakeItFrom.com*, 30-May-2020. [Online]. Available: https://www.makeitfrom.com/material-properties/60-Palladium-40-Silver-Electrical-Contact-Alloy. [Accessed: 27-Apr-2023].
- [18] ASTM D5470-06, Standard Test Method for Thermal Transmission Properties of Thin Thermally Conductive Solid Electrical Insulation Materials, ASTM International, 2006, DOI: 10.1520/D5470-06.

Appendix 1

Air vs Water Pumping Power Calculations

Material Properties: rho (kg/m^3) mu (Pa-s) C_p	Air 1.225 0.0000181 1000	Water 1000 0.00089 4184	Dimensions: Diameter (m) Length (m) Height (m)	Air 0.00635 0.3 0.05	Water 0.0127 3.3 N/A 0.0001266
			Area_cross (m^2)		7
Temperature Rise Allowed	10	10	sigma	0.5	N/A
Heat in (W)	4000	4000 0.0956022	Length_2 (m)	0.55	
M_dot (kg/sec)	0.4 0.3265306	9 9.5602E-	lambda	0.0635	
$G (m^3/sec)$	1	05			
Calculations (Water)			Calculations (Air)		
(,	0.7547164		,	23.7476808	
Velocity (m/s)	2		Velocity (m/s)	9	
D1.4	10760 540		D arm alda	10205.9266	
Reynolds Friction Factor f	10769.549		Reynolds	7 0.00462908	
(moody charts)	0.025		L *	4	
Delta Pressure	3700.1372		_	0.00216666	
(Pa)	1		Friction Factor f	6	
Pumping Power	0.3537416		E	0.00540711	
(W)	1		F_app K c	0.00540711 0.315	
			K_e	0.5625	
				656.063288	
			Delta Pressure (Pa)	4	
			Pumping Power (W)	214.224747 2	

Heat Transfer of the heat into the flow of air or water is equal to mass flowrate times specific heat of the fluid times the temperature difference between the inlet and outlet of the flow.

$$Q = \frac{dm}{dt} * C_p * (T_{out} - T_{in})$$

Pumping Power W is equal to pressure drop P times volumetric Flow rate G as seen in, W = P * G

Raw Thermal Resistance Data from TIM Tester rig

Run 1 (g): 5.8151 3.0621 2.4942 2.2113 1.8008 Run 2 (r): 5.2972 3.2377 2.4524 2.3887 2.0691 Run 3 (c): 5.8884 3.3545 2.3782 1.8981 1.5151 Run 4 (m): 5.9566 3.2180 2.2129 1.7885 1.4414

Compressibility Curve model in Fig. 14

Linear model Poly3:

 $f(x) = p1*x^3 + p2*x^2 + p3*x + p4$

Coefficients (with 95% confidence bounds):

p1 = 1.121e-06

p2 = -0.0001454

p3 = -0.0004657

p4 = 0.9974

Pressure Proximity Rig

Parts

Component	Website	Part number	Qty.	
Aluminum Plates	Mcmaster	9057K13		2
Steel Braces	Mcmaster	9517K431		2
Cold Plate	Digikey	684-ATS-TCP-1021-ND		1
Thin Aluminum Plate	Mcmaster	9057K124		1
Resistors	Mouser	588-TGHPVR500KE		4
Pump	Pumpvendor	JS 10-24489-03		1

PPR CAD Link

 $\frac{https://cad.onshape.com/documents/0a21cf869a49f27240cee911/w/0225437a76c18fdb6f314a78/e/2fb07c87ca1cfce4f2da79a5}{(a)}$

Simscale CFD Simulation Link

 $\underline{https://www.simscale.com/projects/jchalfant/ppr_runs_project}$